The thermal imprint of continental breakup during the formation of the South China Sea

Michael Nirrengarten, Geoffroy Mohn, Andrea Schito, Sveva Corrado, Laura Gutiérrez-García, Stephen Alan Bowden, Frank Despinois

The thermal imprint of continental breakup during the formation of the South China Sea

Michael Nirrengarten[1], Geoffroy Mohn[1], Andrea Schito[2], Sveva Corrado[2], Laura Gutiérrez-García[1], Stephen Bowden[3], Frank Despinois[4]*

1 Département Géosciences et Environnement, Université de Cergy-Pontoise, Cergy-Pontoise, France
2 Università degli Studi di Roma Tre, Dipartimento di Scienze, Sezione di Scienze Geologiche, Largo San Leonardo Murialdo 1, 00146 Rome, Italy
3 Department of Geology and Petroleum Geology, University of Aberdeen, Aberdeen AB24 3UE, UK
4 Total SA Frontier Exploration R&D Program, CSTJF, Pau, France

***Corresponding author:**
Michael Nirrengarten
michael.nirrengarten@u-cergy.fr
Laboratoire GEC, Université de Cergy Pontoise
1 rue Descartes
95000 Neuville-sur-Oise, France

Keywords: Continental breakup, thermal evolution, SE China distal margin, IODP, organic petrography, Raman spectroscopy, biomarker analysis

Abstract

The stretching of continental lithosphere results in asthenospheric upwelling, raising of isotherms, melting during decompression and eventually seafloor spreading. The thermal maturity of overlying sedimentary organic matter from these settings would be expected to be distinctly altered by these processes, however this is still poorly constrained and quantitatively unexplored. International Ocean Discovery Program (IODP) Expeditions 367-368 cored sediments at the Continent Ocean Transition (COT) on the Northern Margin of the South China Sea (SCS). From two settings at the South East China COT we measured and modelled thermal maturity in pre-/syn- to post-rift sediments making use of a range of thermal maturity parameters. Various heat-flow evolutionary scenarios were investigated, with notable jumps in thermal maturity for sediments corresponding to different depositional packages. In order to match observations of thermal maturity, it was found that the deeper and likely pre-rift sediments were heated to temperatures as high as 200°C during initial break up. Achieving this temperature for the deeper sediments requires that significant additional heat be imparted at shallow depths (e.g. exposure to at least the far-field effects of a magmatic intrusion or subsurface expressions of volcanism). The post-rift sediments have lower thermal maturities which are likely due to limited burial and the absence of late post-rift magmatism. The comparison of the SE China COT with other margin examples highlights some parameters controlling the thermal evolution and its record.

1. Introduction

The thermal structure of rifted margins depends on the amount of thinning of the continental lithosphere, the time elapsed since breakup (i.e. cooling duration), the amount of radiogenic-heating supplied by the residual continental crust and lithospheric mantle (McKenzie, 1978; Sclater et al., 1980). During continental extension isotherms initially rise, but this period of heating is followed by progressive cooling as the rifted continent transfers heat by conduction to overlying sediment (Royden et al., 1980). Modelling this evolution with accurate stratigraphic and petrophysical properties, e.g. thermal conductivity, allows prediction of the thermal evolution of extensional systems. When applied within a basin model where calibration is used, modelling processes such as hydrocarbon generation allows dynamic parameters such as pore pressure to be predicted (Peters and Nelson, 2012). However, at many Continent Ocean Transitions (COT), current heat-flow measurements differ greatly from predictions (Lucazeau et al., 2008; Nissen et al., 1995) highlighting the lack of calibration for thermal modelling in such settings. Deep boreholes, seismic images, geophysical data and field studies at COT reveal complex deformation modes and associated magmatism and hydrothermal fluid circulation (Jagoutz et al., 2007; Larsen et al., 2018a; Manatschal, 2004), all of which impact to different extents thermal evolution and heat transfer mechanisms during and after rifting.

Previous studies have investigated the thermal maturity of organic matter dispersed in sediments at COT using deep borehole data (Peace et al., 2017; Pross et al., 2007), or sedimentary successions preserved along fossil margins stacked in mountain belts that escaped pervasive syn-orogenic metamorphic overprint (Clerc and Lagabrielle 2014; Lescoutre et al., 2019). However, at COTs basin models are often unreliable due to the lack of distal deep

boreholes, the lack of samples to provide measurements to calibrate models and the difficulty of incorporating fluid flow and igneous events in basin models (Gardiner et al., 2019). Here we report new thermal maturity data from two holes located at the SE China COT, where petrophysical data, heat-flow measurements and thermal maturity observations better constrain the thermal evolution. The intent is that future work can compare the SCS rifted margin to others in order to construct better thermal models for COT.

Sites U1499 and U1502 were drilled during IODP Expeditions 367-368 on the SE China COT. Holes at these sites penetrate sedimentary, magmatic and hydrothermally altered sediments and rocks located at the most distal SE China continental margin (a location with extreme lithospheric thinning and crustal thickness <10 km). This unique dataset permits the investigation and modelling of the *in situ* thermal history of pre- syn- and post-rift sediments and from this can be deduced the thermal effects of the rifting-processes that formed the South China Sea.

2. Geological setting and structure of the SE China distal margin

The SE China margin is located along the northern edge of the SCS oceanic basin (Fig. 1) that propagated from NE to SW between ~33 Ma and ~15 Ma (Briais et al., 1993; Taylor and Hayes, 1983). Previous studies (e.g. Franke et al., 2014) complemented by IODP Expedition results (Larsen et al., 2018b) reported a major Eocene rifting phase followed by early Oligocene breakup (~30 Ma) on the SE China distal margin. The investigated segment of the distal SE China margin is ~90 km long (Fig. 1B, Fig. 2) and presents a progressive thinning of the continental crust which eventually tapers off passing abruptly in space and time to igneous oceanic crust (Larsen et al., 2018b) (at ~85 km on Fig.2b). IODP expeditions 367-368 and 368X penetrated the acoustic basement at 6 locations. The top of the acoustic basement is

105 recognized as the Tg-reflector (Fig1B-2) and corresponds to the base of the Cenozoic
106 succession (Zhou et al., 1995). Along this segment, distinct tectonic structures were
107 recognized from the continent to the ocean; namely the Outer Margin High (OMH), and the
108 ridges A, B and C.

109 The OMH (to the northwest in the profile of Fig. 2) is formed by a 15 to 20 km thick continental
110 crust that includes pre-rift sediments and metamorphic rocks sampled below the Tg reflector
111 at Sites U1501 and U1504, respectively. The COT presents a progressive thinning of the
112 continental crust characterized by a gradual rise of the Moho up to the 7-8 km thick ridge A
113 (Fig. 2). This ridge was sampled at two sites (U1499 and U1502). Highly altered Mid-Ocean
114 Ridge Basalts (MORB) are recovered at Site U1502 (Fig. 3), whereas 40 km to the west, at Site
115 U1499 pre- to syn-rift clastic sediments are present confirming the continental nature of ridge
116 A (Fig. 2) (Larsen et al., 2018a; Nirrengarten et al., in press).

117 Ridges B and C are 7 km thick and represent landward rotated fault blocks penetrated
118 respectively by sites U1500 and U1503. At both of these sites MORB with pillow structures are
119 present and here a magnetic anomaly C11n dates the crust to 30.0 Ma (Larsen et al., 2018a
120 and Fig. 2) and constrains the breakup age to early Oligocene. Seismic observations, gravity
121 modelling and the analysis of crustal bulk densities further confirm the location of the
122 continent ocean boundary between ridges A and B (Nirrengarten et al., in press). As a result,
123 ridge A represents the last remnant of continental crust in the investigated segment, recording
124 extreme lithospheric thinning and the onset of MORB magmatism during final rifting.

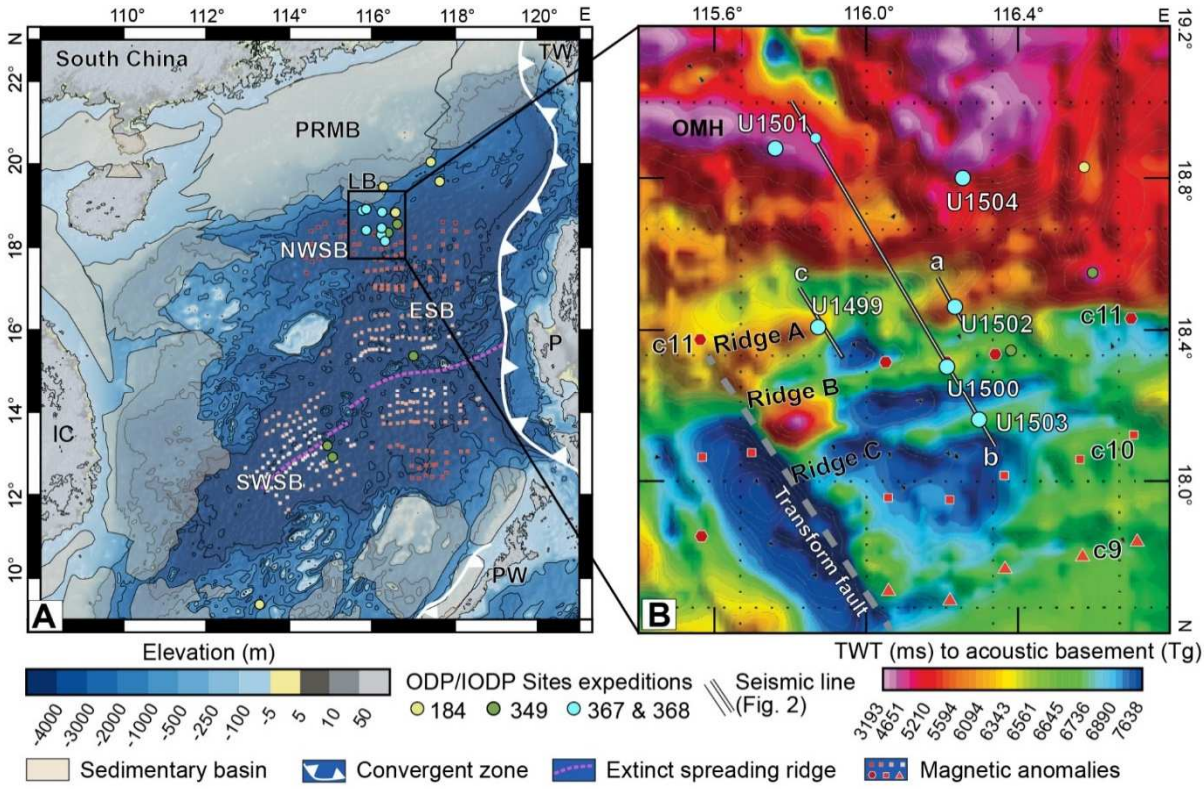

Fig. 1 Topographic map of the SCS (Amante and Eakins, 2009) showing the oceanic magnetic anomalies (Briais et al., 1993) and the main tectonic features.ESB, East sub-basin; IC, Indo-China; LB, Liwan Basin; NWSB, Northwest sub-basin; P, Philipines; PRMB, Pearl River Moouth Basin; PW, Palawan; SWSB, Southwest sub-basin; TW, Taiwan B) Zoomed map of the top acoustic basement (Tg reflector)(Larsen et al., 2018b) on the margin segment penetrated by IODP Expeditions 367 & 368 and 368X. Both maps are projected in geographic coordinate system WGS 84. The two sites on Ridge A (U1499 and U 1502) are separated by 40 km distance. Location of seismic lines shown in Fig. 2

3. Structure and sedimentary sequence of ridge A

Ridge A can be mapped across the margin's entire segment (Fig. 1) (~90 km). This basement high has significant morphological variations, characterized by a narrow and sharp basement geometry to the NE (Site U1502), passing to a rounded and blurred shape, 40 km to the SW (Site U1499) (Fig.2). Based on seismic and borehole data, ridge A is interpreted as the last rotated continental fault block bounded by a major oceanward normal fault that juxtaposed the initial oceanic crust (Fig. 2).

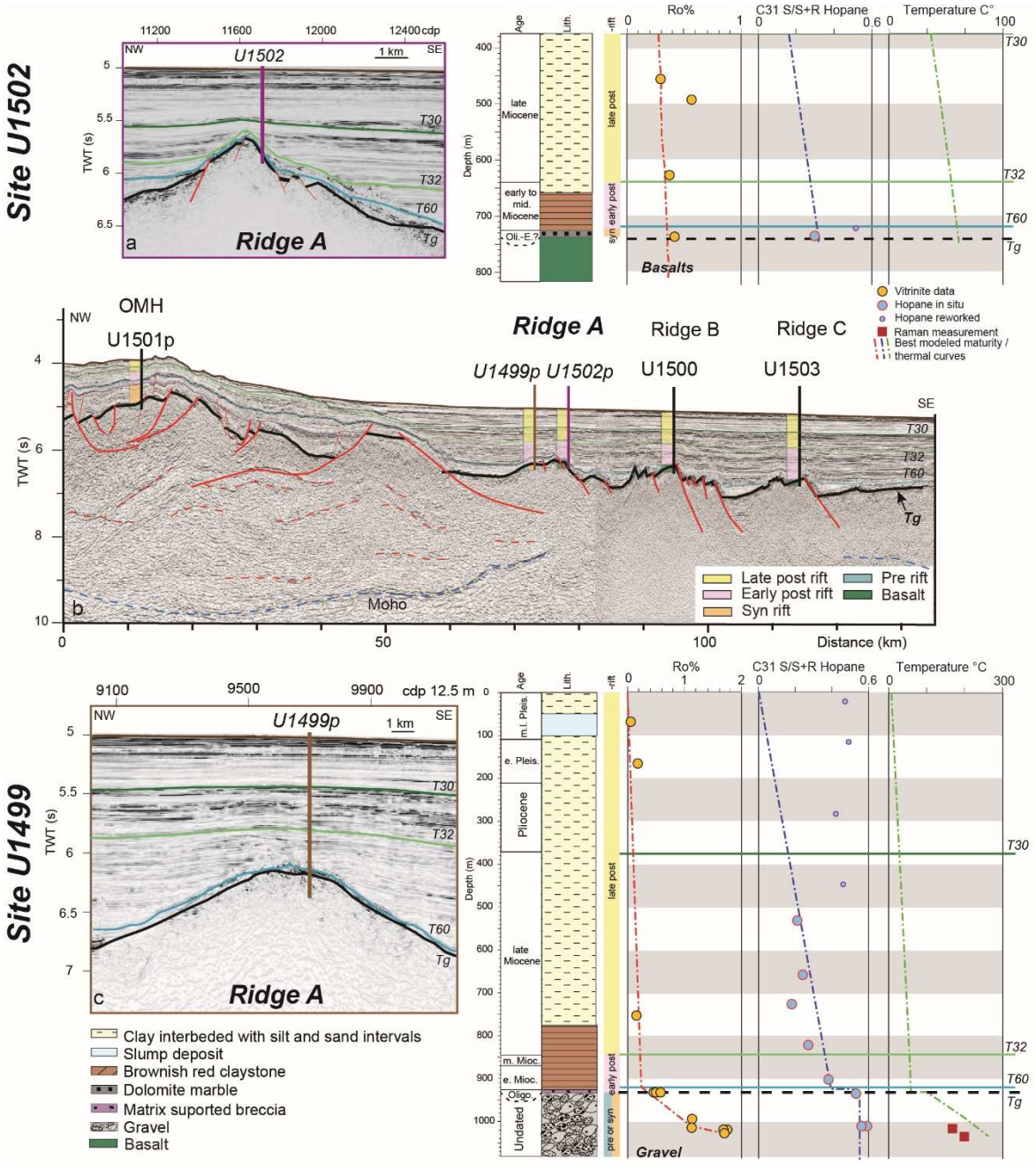

142

143 **Fig. 2** a) Zoomed seismic section on the location of Site U1502 with the stratigraphic
144 column, the thermal maturity data and calculated temperatures recorded at Site U1502; b)
145 Seismic section crossing the SE China COT (Larsen et al., 2018b) OMH: Outer Margin High; c)
146 Zoomed seismic section on the location of Site U1499 with the stratigraphic column, the
147 thermal maturity data and calculated temperatures recorded at Site U1499. Measured
148 thermal maturity data are vitrinite reflectance (% Ro) and C31 αβ hopane parameter
149 [22S/(22S +22R)], whereas paleo-temperatures are determined by Raman spectroscopy (°C).
150 Dashed curves represent the best-modelled thermal maturity or maximum paleo-
151 temperature profiles (see Fig.6).

152

153 Based on biostratigraphy and seismic architecture, the sedimentary succession of this area is
154 divided into four units late post-rift (recent to the mid/early Miocene boundary 0-11.6 Ma),
155 early post-rift (Mid Miocene to breakup time in Oligocene 11.6-30 Ma), syn-rift (early
156 Oligocene to Eocene) and pre-rift (undated, Fig. 2). Post-rift lithologies are similar at Sites
157 U1499 and U1502, composed of alternating clay, silt and sand with variable amount of
158 nannofossils. Located on this basement high, both sites show a very low early post-rift
159 sedimentation rate of 8-10 mm.kyr^{-1} (Larsen et al., 2018b) that increases to 39-80mm. kyr^{-1}
160 during the late post-rift stage. This early to late post-rift sequences are delimited by the T32
161 reflector in seismic profiles. In contrast, the pre-Miocene (below T60 reflector) early post-rift
162 and syn-rift stratigraphic record differs significantly between the two sites.

163 *3.1 Early post-rift to syn- or pre-rift succession at Site U1499*

164 At Site U1499, 927 meters below sea floor (mbsf) the early Miocene (early post-rift) reddish
165 gray clay-rich chalk (Sun et al., 2018) passes to a 60 cm thick level containing iron-manganese
166 nodules. Below, a 4 m thick matrix-supported breccia (Fig. 4) is dated from ~26 to ~30 Ma
167 (Oligocene) representing the earliest post-rift sediments and the last age datum in the well
168 (Sun et al., 2018). This breccia is composed of pebble size polymict angular sandstone clasts
169 in a nannofosil rich claystone matrix (Fig.4 (Sun et al., 2018)). This unit at Site U1499 is coeval
170 to sediments intercalated within pillow basaltic lava of the first igneous oceanic crust sampled
171 at U1500 (Larsen et al., 2018a) (Fig. 2). Below, cores penetrated the Tg reflector and are
172 composed of 148 meters of undated gravels representing either syn- or pre-rift sequences.
173 These gravels comprise polygenic cobble-sized clasts of former sandstones and siltstones but
174 igneous clasts are not observed. Also present in this succession are poorly lithified clayey silt
175 or silty sand intervals which while possessing laminae rich in organic matter, have low

carbonate content and do not contain calcareous nannofossils (Sun et al., 2018). These sands and silts are interpreted as the matrix for the gravel (Fig.4). It is likely that the matrix is under represented in core due to its washout during drilling operations. Clasts within the overlying earliest post-rift matrix supported breccia (Fig.4) are angular and comprise lithologies that are the same as the underlying gravel, indicating a possible reworking during the late syn-rift and earliest post-rift time interval.

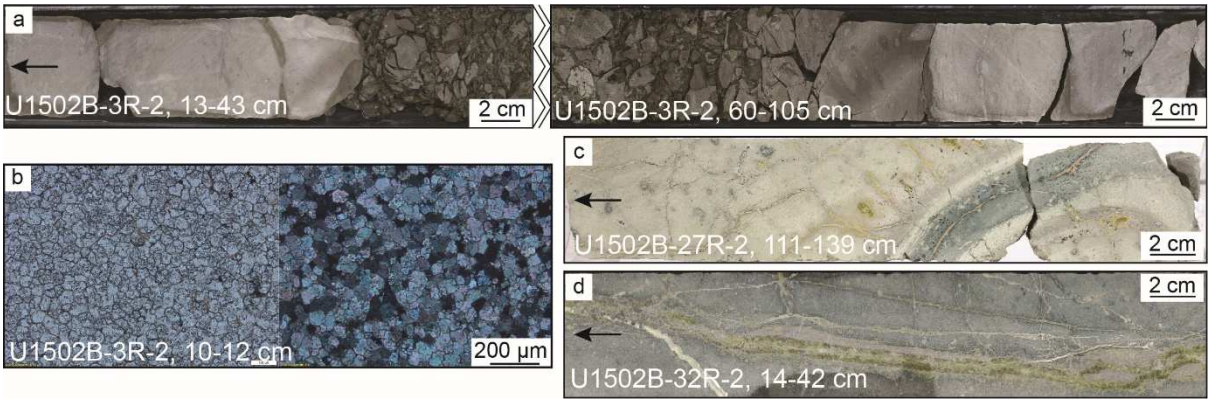

Fig. 3 Photographs and photomicrographs of the Sites U1502: a) Dolomitic marble alternating with meta-claystone located at less than 10m from hydrothermally altered MORB (U1502B-3R-2). b) Cross polarized and analysed photomicrography of the fully recrystallised dolomitic marble (U1502B-3R-2). c) Highly altered basalt with relic of pillow structures (U1502B-27R-2). d) altered basalt crosscut by branched epidote-calcite veins (U1502B-32R-2).

3.2 Early post-rift to syn-rift succession at Site U1502

At Site U1502, the first 375 meters of Pleistocene and Pliocene sediment was not cored. At 739 mbsf, drilling penetrated early post-rift late Oligocene greenish gray biosiliceous claystone. The claystone is overlain by pre-late Oligocene light gray dolomitic marble or limestone that is intercalated with clays that have igneous clasts, meta-claystones and sandstone (Larsen et al., 2018c) (Fig. 3). Here the thin syn-rift sequence is about ~10 m thick (Fig. 3). The dolomitic marble is composed of ~95% recrystallized euhedral dolomite (Larsen

196 et al., 2018c) (Fig. 3), which indicates a pervasive hydrothermal transformation of the initial
197 protolith (Machel, 2004).

198 Underlying the syn-rift sediments, and beneath the Tg reflector at 749 mbsf is an igneous
199 basement composed of basaltic breccias, brecciated-basalts with a jigsaw-like fit indicating
200 hydraulic fracturing (Fig. 3). Hydrothermal fluid circulation is confirmed by the numerous veins
201 with variable composition, from silica- and carbonate-rich to epidote-rich. The veins are
202 interconnected networks and have branched geometries (Fig. 3). Despite hydrothermal
203 alteration, pillow structures are still visible (Fig.3) and the geochemical signature of the bulk
204 rock is typical for a MORB (Larsen et al., 2018c).

205 Diagenesis of this sedimentary sequence records the thermal history of the distal rifted
206 margin, in the following section we describe the sampling strategy of the cores and the
207 analyses we conducted to determine the temperature history.

208 ***4. Approach and analytic methods***

209 *4.1 Sampling strategy*

210 Sampling was guided by total organic carbon content (see Sun et al., 2018 and supplementary
211 information), with preference given to organic matter rich intervals most likely to yield high
212 quality data (e.g. those with a TOC > 0.5 %, SI 1). The deepest units at the base of U1499 were
213 sampled at a greater frequency because of their importance for capturing syn-rift thermal
214 history), with both the matrix and the clasts of the pre- to syn-rift breccias sampled.

215

216 *4.2 Vitrinite reflectance*

217 Vitrinite reflectance Ro% is commonly used in the oil industry to evaluate the thermal maturity
218 of organic matter dispersed in sediments (Suárez-Ruiz et al., 2012). This method is based on

219 the microscopic observation of a single class of solid organic matter (huminite-vitrinite
220 maceral group) whose molecular reorganization due to increasing temperature through time
221 results in an increase of its reflectivity (Tissot and Espitalié, 1975). Samples for vitrinite
222 reflectance were analyzed in reflected, non-polarized, monochromatic light (λ=546 nm) under
223 oil immersion (v=1.518) using a Zeiss Axioskop MPM400 microscope equipped with MPS 200
224 system by J&M Analytik AG. Standardization was performed using a Spinel with relative
225 reflectance (Rr) of 0.426%, Saphir with Rr of 0.585%, YAG (Yttrium-Alluminium-Garnet) with
226 Rr of 0.905% and GGG (Gadolinium-Gallium-Garnet) with Rr of 1.72.
227 Thermal maturity of each sample were defined according to the ASTM standard D7708-14.
228 Here we take the immature stage of hydrocarbon generation to be indicated by Ro% values
229 less than 0.5%, the early stages of oil and hydrocarbon generation to correspond to Ro% values
230 between 0.5 and 0.7% and the late stages of oil generation to occur between 0.8 and 1.35%.
231 Histograms of the vitrinite reflectance are presented in SI 2-3.
232
233 *4.3 Raman spectroscopy*
234 Raman spectra of carbonaceous matter provide a geothermometer across both metamorphic
235 (T> 200°C) (Beyssac et al., 2002; Lahfid et al., 2010) and diagenetic temperature conditions
236 (50-200°C) (Lünsdorf and Lünsdorf, 2016; Schito et al., 2017; Schmidt Mumm and Inan, 2016;
237 Wilkins et al., 2014), as well as within the thermal aureoles of magmatic intrusions (Muirhead
238 et al., 2017). Micro-Raman spectroscopy was carried out using a Jobin Yvon LabRam system in
239 a backscattering geometry. Data were collected in the first order Raman spectrum over the
240 range 1000–2000 cm^{-1} using a 600 grooves.mm^{-1} spectrometer grating and CCD detector and
241 Neodimium-Yag green laser (532 nm) as a light source. Laser-induced degradation of kerogen
242 and fluorescence-background signals were minimised by maintaining laser power below 0.4

mW. Using optical filters, the Raman backscattering was recorded with an integration time of 20s for 6 repetitions. Each fragment was analysed with a 2µm diameter spot using a 20× or a 50× optical power objective.

Raman analyses were only performed for Site U1499, and were performed on splits of the same samples used for vitrinite reflectance. During sample preparation analyses avoiding polishing with less than 0.1 µm slury according to recommendation from Lünsdorf and Lünsdorf (2016). Measurements were taken on both vitrinite fragments and on the organic matter within the matrix (amorphous organic matter). We adopted two methods to deconvolve Raman spectra to obtain maximum paleo-temperature data. The first method is particularly suitable for low maturity samples and is based on a separate deconvolution of the D and G band regions (Fig. 4). After a linear baseline correction, the position, width and integrated areas of the D and G band are measured separately and converted into vitrinite reflectance equivalent (Ro_{eq}%) and maximum temperature is obtained following a multi-parametric equation according to (Schito and Corrado, 2018). Spectra indicating higher thermal maturity levels were analysed using an automatic approach, based on the D and G bands parameters, which directly returns the maximum paleo-temperatures acquired during burial (Lünsdorf and Lünsdorf, 2016).

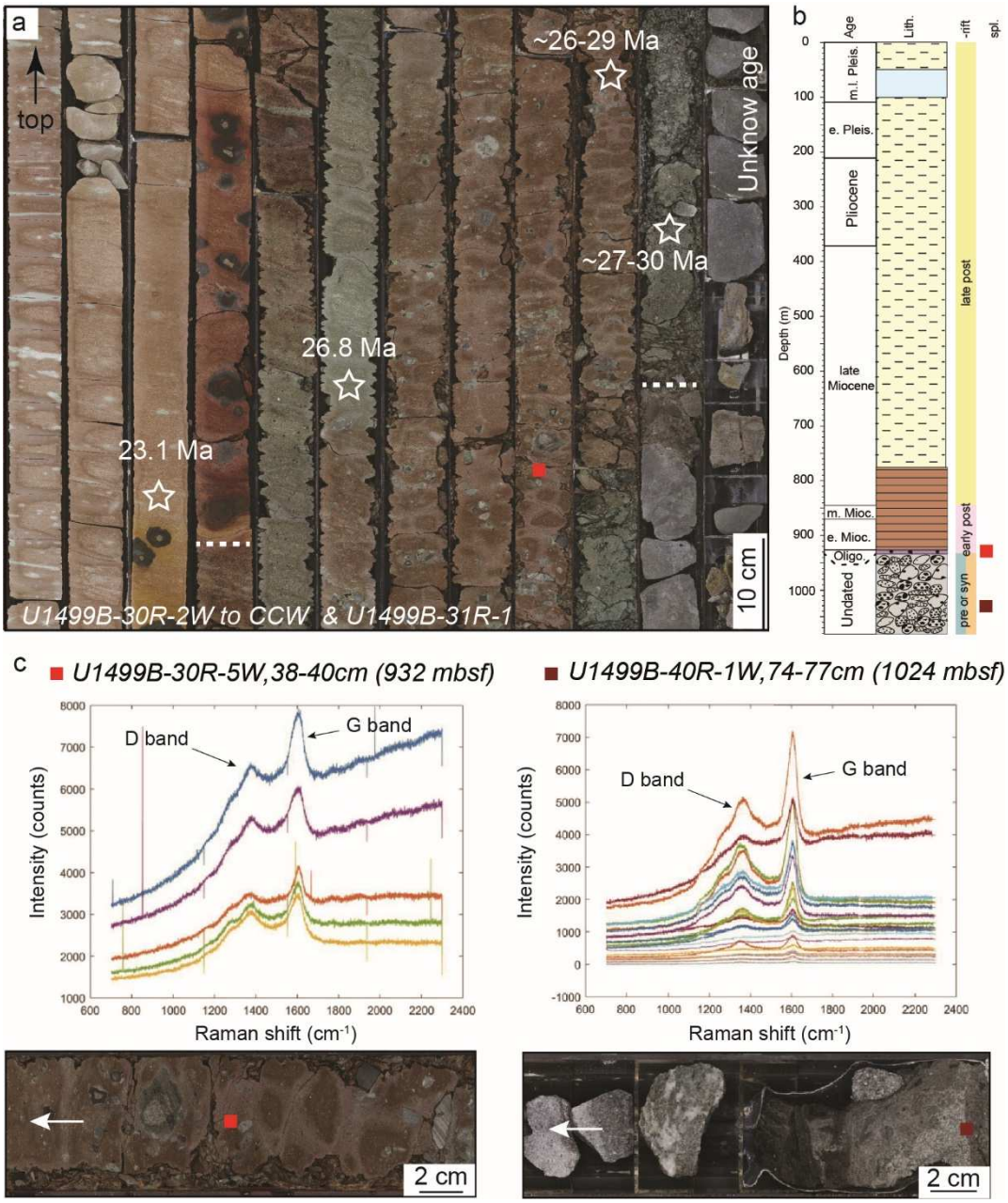

Figure 4: a) Core U1499B-30R and 31R. The transitions between Early Miocene clay rich chalk (early post-rift), Oligocene matrix supported breccia (earliest post-rift) and undated polygenic gravel unit (pre- or syn-rift?) are marked by the white dashed lines. White stars correspond to the location of the biostratigaphic datum (Sun et al., 2018). b) Stratigraphic column of Site U1499 with the location of the Raman spectroscopy samples. c) Raman spectra collected for sample U1499B-30R-5 and U1499B-40R-1 with corresponding core photo showing sample locations

4.4 Biomarker analysis

Samples for biomarker analysis were solvent extracted using Soxhlet apparatus (5-25 g of sediment or rock was extracted in dichloromethane/methanol 93:7 v/v for 48h). The extract was fractionated using flash mini-column chromatography (silica column; hexane for saturated fraction; 3:1 v/v hexane/dichloromethane for aromatics fraction; 2:1 v/v dichloromethane/ methane for polar fraction). The resulting saturate fraction was analyzed by gas chromatography-mass spectrometry (GC-MS). GC-MS was performed using a 6890N Network GC system interfaced to a 5975 inert mass selective detector. A PTV in injector (300 °C) operating in split less mode was used and the GC temperature program was as follows; 60 °C to 120 °C at 20 °C.min^{-1} then from 120°C to 290°C at 4°C.min^{-1}. The column was Greyhound GC-5 (an HP-5 equivalent phase; 30 m length, 250 µm ID and 0.25 µm film thickness). The MS was operated in sim mode (less than 20 ions with a dwell time less than 40 ms). Compounds were identified by reference to well-characterized samples of bitumen of analogous thermal maturity. Inputs for biomarker thermal maturity parameters were obtained from peak areas measured on the *m/z* 191 ion chromatogram for hopanes and *m/z* 217 ion chromatogram for steranes (Fig.5, Table 3 and SI 4).

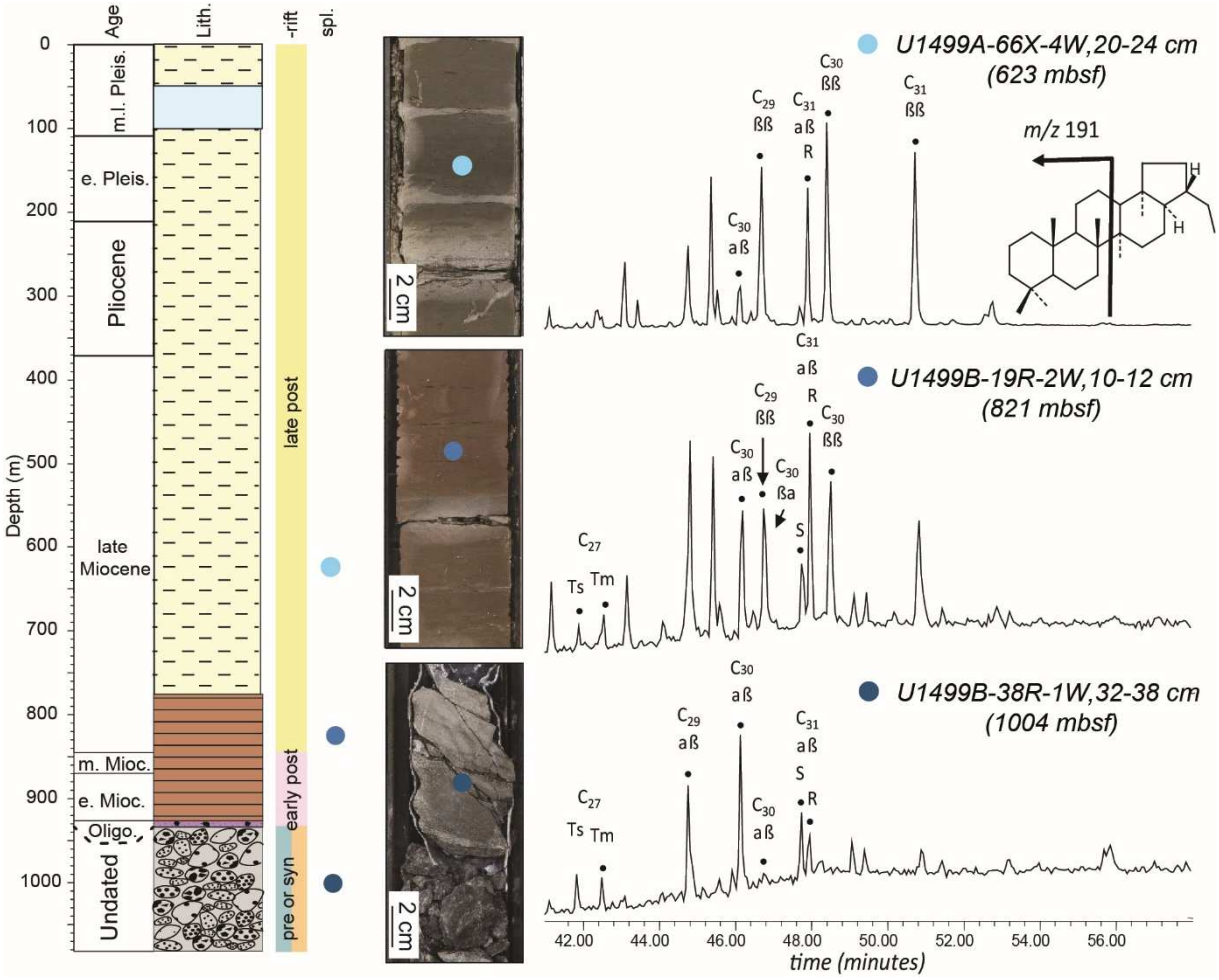

Figure 5: Selected ion chromatograms for *m/z* 191, for samples of Site U1499 and their corresponding core pictures. Carbon number is listed. C_{27}Tm = C_{27} 17α(H) 22,29,30-Trisnorneohopane, αβ = 17α,21β(H) hopane; βα = 17β,21α(H); ββ = 17β,21β(H) hopane; αβ S = 17α,21β(H)22(S) hopane; αβ R = 17α,21β(H)22(R) hopane.

5. Results

5.1 Site 1499

5.1.1 Late post-rift (0-840 mbsf)

Samples from the late post-rift sequence have a relatively low TOC (<1 wt%, Table 1 and SI 1) (Sun et al., 2018). The vitrinite data from 3 samples of the late post-rift sequence (Pleistocene to mid Miocene) show very low thermal maturity values ranging between 0.26 and 0.41 Ro%

297 (in the immature stage of hydrocarbon generation, Fig. 2, Table. 1). Despite very high
298 fluorescence that made analyses difficult, we were able to obtain six Raman spectra from
299 sample U1499B-12R-1W (752 mbsf) that show very low maturity with an average value of
300 Ro_{eq}% of 0.34 and a standard deviation of 0.13 (Table, 2).

301 Biomarker thermal maturity indicators of thermal alteration include both the Hopane 22S
302 (here after referred to as hop-22S) and sterane 20S parameter (See Table 2 and Fig. 5). As
303 Raman and vitrinite reflectance they record a similarly low level of thermal alteration of
304 organic matter in the late post-rift succession (Tables 1,2,3). The strongest assessment of a
305 change in thermal maturity within this interval is obtained from the hop-22S parameter, which
306 changes from 0.11 to 0.25 from 623 to 726 mbsf. This observation represents a slight increase
307 in the parameter above its background level, but is important because the hop-22S parameter
308 has a kinetic model (Mackenzie and McKenzie, 1983), which can be used to constrain thermal
309 history in these sediments.

310 There are instances where thermal maturity parameters are high within the late post-Rift
311 sediment (Table 3), but most of these likely represent allochthonous organic matter as there
312 is no indication of faulting or intrusive activity that might otherwise account for sudden
313 downhole *in situ* changes in thermal maturity within the late post-rift succession. Additionally
314 biomarkers such as sterenes or the proportion of ββ hopanes that are destroyed by exposure
315 to hotter temperatures are still present (Amo et al., 2007; Farrimond et al., 1998), indicating
316 that any high values must be explained by processes that do not involve heating of the host
317 formation (e.g. thermal alteration of the biomarkers occurred prior to burial at the current
318 location).

319 Thus, despite a high present-day heat flow (110 $mW.m^{-2}$), the late-post-rift sediments at site
320 U1499 show a geologically mild thermal history, despite a high rate of burial in a rapidly
321 subsiding basin.

322 *5.1.2 Early post-rift (840-933 mbsf)*

323 The early post-rift is composed of Miocene reddish claystone. In this interval, only biomarker
324 data provided reliable results. Indications of a pre-oil window level of thermal maturity for the
325 early Miocene red claystone are still present in the form of ββ hopanes and a hop-22S value
326 of 0.38 (900mbsf).

327 Below, in the earliest post-rift matrix supported breccia two samples at 932 and 933 mbsf
328 show a thermal maturity at 0.59 and 0.66 Ro% respectively (in the initial portion of the oil
329 window). Additionally, within this interval Raman spectra resolve clearly identifiable D and G
330 bands indicative of organic matter that has experienced catagenesis (Fig. 4 D and G bands with
331 a Roeq of 0.65 % std 0.18 calculated via Schito and Corrado 2018), however there are Raman
332 spectra indicative of a higher thermal maturity, indicating the presence of allochtonous
333 organic matter (not included in the calculation of Roeq).

334

335 *5.1.3 Gravel unit (syn- or pre-rift?) (933-1082 mbsf)*

Name	Offset (cm)	Depth (mbsf)	TOC %	Ro %	Std (Ro%)	Number of measure	Lithology	Age
U1499								
U1499A-8H-4W	130-134	70.01	1.36	0.26	0.033	18	Sandy silt	Late Pleistocene
U1499A-19X-4W	22-24	167.12	0.5	0.41	0.035	10	Clay with silt	Early Pleistocene
U1499A-48X-5W	18-22	449.72	0.49	n.d.	n.d.	0	Foraminiferal sand	Late Miocene
U1499B-12R-1W	30-34	752.32	0.44	0.29	0.035	67	Sandstone	Late Miocene
U1499B-30R-5W	38-40	932.22	0.32	0.59	0.046	19	Sandy Claystone with gravel	Oligocene
U1499B-30R-6W	24-26	932.98	no data	0.66	0.042	34	Matrix suported breccia with gravel	Oligocene
U1499B-34R-1W	91-96	966.31	0.23	n.d.	n.d.	0	Gravel sandstone	Oligocene or pre Oligocene
U1499B-37R-1W	115-120	995.64	3.15	1.22	0.066	27	Gravel sandstone	Oligocene or pre Oligocene
U1499B-39R-1W	58-60	1014.45	no data	1.22	0.086	20	Gravel sandstone	Oligocene or pre Oligocene
U1499B-40R-1W	19-23	1023.79	no data	1.76	0.08	52	Silty sand with clasts	Oligocene or pre Oligocene
U1499B-40R-1W	78-81	1024.38	2.19	1.77	0.092	45	Silty sand with clasts	Oligocene or pre Oligocene
U1499B-41R-1W	39-46	1033.69	0.61	1.74	0.052	22	Silty sand with clasts	Oligocene or pre Oligocene
U1499B-44R-1W	17-21	1062.64	no data	1.83	0.069	20	Gravel siltsone	Oligocene or pre Oligocene
U1502								
U1502A-10R-5W	56-60	457.98	0.3	0.29	0.07	6	Clay with nannofossils	Late Miocene
U1502A-14R-3W	12-16	493.32	no data	0.57	0.07	3	Clay	Late Miocene
U1502A-28R-2W	46-50	626.15	0.53	0.38	0.06	16	Silty clay	Middle Miocene
U1502B-4R-1W	47-49	739.1	0.27	0.43	0.054	7	Dolomitic sandstone	Oligocene

Table. 1 Vitrinite reflectance data for Site U1499 and U1502

In the gravel unit, TOC values are highly variable between the different clasts and the matrix with the highest TOC content being 4.8 wt% (Sun et al., 2018). Vitrinite reflectance data in this oldest (pre-30 Ma) and deepest sampled unit are anomalously high when compared to the post-rift sequence. This gravel unit is characterized by an extremely rapid downhole increase in thermal maturity from 1.22 to 1.83 Ro% (from the upper part of the oil window to the gas window) across a 67m thick section (respectively at 995 and 1062 m bsf) (Fig. 2). Thermal maturity of organic matter measured in the cobble-sized clasts is equivalent to that of the clay and silt matrix. This is an important observation because it indicates that both the large clasts that are most likely to preserve reworked organic matter, and the matrix that is likely to contain autochthonous organic matter have shared the same thermal evolution. Therefore, there is no evidence of a previous and more severe thermal history, inherited from the reworked sediment, recorded within the clasts.

It is also important to note that over a relatively short distance of 130 m, from the early post-rift Oligocene matrix-supported breccia Unit to the deepest sample of the syn- to pre-rift gravel Unit there is a large increase in thermal maturity (increase of 1.17 %Ro from U1499B-

30R-6W, 932.98 mbsf to U1499-44R-1W 1062.64 mbsf in Table 1). In this unit the hop-22S parameter is above 0.55 and exceeds the oil window and would not therefore record further thermal alteration (Mackenzie and McKenzie,1983). Homogeneous Raman spectra (Fig. 4) were measured using the method presented by Lündsdorf et al., 2017. These samples showed maximum paleo-temperatures for a sandstone clast sample at 995 mbsf are 193 ± 38°C (U1499B-37R-1W), and for a matrix sample at 1024 mbsf are 210 ± 35°C (U1499B-40R-1W)(Fig. 2-4 and Table 3). In synthesis, the three different analytical techniques record a rapid increase in maximum paleo-temperatures and thermal maturity experienced by organic matter dispersed in the gravel unit.

Name	Offset (cm)	Depth (mbsf)	Number of measure	Raman temperature (°C)	Std (°C)	Ro% Raman equivalent	Std (Roeq%)	Age
U1499								
U1499B-12R-1W	30-34	752.32	6			0.34	0.13	Late Miocene
U1499B-30R-5W	38-40	932.98	5			0.65	0.18	Oligocene
U1499B-37R-1W	115-120	995.64	13	193	38			Oligocene or pre Oligocene
U1499B-40R-1W	74-77	1024.38	21	210	35			Oligocene

Table 2: Raman spectroscopy results. Ro% equivalent is determined based on the method developed by Schito and Corrado (2018) and temperature results from the spectra analysis of (Lünsdorf and Lünsdorf, 2016)

U1499													
U1499A-3H-5W	70-72	23.72	Post-Rift†	4.98	0.2	0.8	99	0.40	0.47	0.21	-	-	-
U1499A-7H-5W	70-72	61.68	Post-Rift	1.70	86	0.00	14	0.49	0.63	0.22	-	-	-
U1499A-13H-4W	70-72	117.25	Post-Rift	0.27	12	12	76	0.39	0.54	0.42	-	-	-
U1499A-21X-4W	60-62	186.92	Post-Rift	0.32	50	< 0.1	50	0.43	0.61	0.10	-	-	-
U1499A-27X-6W	67-69	248.19	Post-Rift	0.14	14	10	76	0.36	0.49	0.24	-	-	-
U1499A-31X-4W	38-42	283.72	Post-Rift	0.16	55	12	33	0.31	0.42	0.30	-	-	-
U1499A-48X-3W	106-108	447.78	Post-Rift	0.22	11	11	78	0.49	0.46	0.21	-	-	-
U1499A-57X-1W	65-68	531.68	Late-post rift	0.42	3	11	86	0.14	0.21	0.41	-	-	-
U1499A-66X-4W	20-24	623.04	Late-post rift	2.05	25	13	62	0.23	0.11	0.51	0.18	26	0.21
U1499B-2R-3W	5-10	657.81	Late-post rift	1.03	22	56	22	0.07	0.24	0.44	-	-	-
U1499B-9R-3W	80-85	726.39	Late-post rift	1.04	17	17	66	0.32	0.18	0.49	0.08	13	0.06
U1499B-19R-2W	10-12	821.37	Late post-rift	0.11	50	25	25	0.40	0.27	0.33	0.22	33	0.42
U1499B-27R-4W	7-8	900.56	Early post-rift	1.46	40	40	20	0.22	0.38	0.32	0.25	25	0.39
U1499B-30R-1W	2-5	933.65	Gravel	0.25	42	29	29	0.65	0.53	0.03	0.37	23	0.71
U1499B-38R-1W	32-38	1004.59	Gravel	0.11	10	10	80	0.51	0.56	0.03	0.41	54	0.62
U1502													
U1502A-38R-5W	116-118	726.29	Early post rift	1.16	10	10	80	0.61	0.51	0.20	0.45	32	0.35
U1502A-40-4W	90-94	744.75	Syn rift	3.39	10	10	80	0.15	0.26	0.45	0.11	25	0.12

*Sample names follow IODP nomenclature; †Post-Rift sediments evidence reworking as discussed in text; EOM = extractable organic matter mg extract/g sed (dry); CC composition = composition based on silica gel column chromatograpgy, Sats = saturate hydrocarbons, Aros Aromatic Hydrocarbons, Polars = polar compounds; Hopane thermal maturity parameters calculated using abundances as follows, Ts/Ts+Tm = C_{27} 18α(H)-22,29,30 trisnorheopane/C_{27} 18α(H)-22,29,30 trisnorheopane + C_{27} 17α(H)-22,29,30 trisnorhopane, Hop 22S = C_{31} 17α,21β(H) 22S/C_{31} 17α,21β(H) 22S + C_{31} 17α,21β(H) 22R hopane, ββ Hop = C_{30} 17β,21α(H)/C_{30} 17β,21α(H) + C_{30} 17α,21β(H) hopane; Sterane thermal maturity parameters calculated as follows, Ster 20S = C_{29} 5α,14α,17α(H) 20S/ C_{29} 5α,14α,17α(H) 20S + C_{29} 5α,14α,17α(H) 20S sterane, % αββ = 100 × C_{29} 5α,14β,17β(H) 20S & 20R/ C_{29} 5α,14β,17β(H) 20S & 20R steranes + C_{29} 5α,14α,17α(H) 20S & 20R steranes, P.I. (Pregnane Index) = C_{21}+C_{22} pregnanes / C_{21} & C_{22} pregnanes + C_{29} 5α,14β,17β(H) 20S & 20R steranes + C_{29} 5α,14α,17α(H) 20S & 20R steranes. Data are plotted graphically in SI 5.

Table 3: Biomarker thermal maturity parameters

5.2 Site 1502

5.2.1 Post rift

At site U1502, the post-rift section has TOC values lower than <0.7 wt% (Larsen et al., 2018c) and only three samples provided reliable vitrinite reflectance data. No reliable Raman analyses

were obtained. The early and late post-rift sequences show a low themal maturity with Ro% values from 0.29% to 0.38%. An anomalously high value of 0.57 Ro% at 493.32 mbsf has been interpreted as reworked dispersed organic matter. The upper part of the late rift succession at Site U1499, the hop-22S parameter is high (0.51 at 626 mbsf (Table 3) and indicates reworking of soluble organic matter during post-rift evolution

5.2.2 Syn rift

The syn-rift dolomitic marble has a vitrinite reflectance value of 0.43 Ro% at a depth of 739 mbsf indicating a pre-oil window thermal maturity, an observation consistent with a hop-22S value of 0.26 recorded at 744 mbsf that also indicates a pre-oil window thermal maturity. The close correspondence of these two independent measures of thermal maturity for the syn-rift succession at U1502 indicates that the data likely represent a true *in situ* thermal maturity. Although this overall level of thermal maturity for the syn-rift succession at U1502 is low with respect to hydrocarbon generation, for its relatively shallow depth (< 800 mbsf) the syn-rift of U1502 is thermally mature (e.g. more thermally altered than an equivalent depth at U1499).

6. Modelling

To determine the thermal evolution of the SE China COT at ridge A, 1D basin models were produced using BasinMod 2D (Fig. 6). Basin models integrated porosity and thermal conductivity data measured for U1499 and U1502 (Larsen et al., 2018b). Different heat-flow scenarios were investigated. The first scenario used a constant heat-flow through time (Fig. 6). Temperature measurements acquired during piston coring at site U1499 give a present-day geothermal gradient of 93°C/km and an estimated heat flow of 110 $mW.m^{-2}$ calculated using measured thermal conductivities of the sampled-sediments (Sun et al., 2018). The constant heat-flow model has a good correlation with the late post-rift section (above Tg) at

both sites although it is unable to match the higher thermal maturity values in the earliest post-rift and in the gravel unit at Site U1499 (Fig. 6).

The second model is based on the depth independent lithosphere thinning model from McKenzie (1978), and referred to hereafter as the McKenzie type model. It assumes that heat flow increases due to the extension of continental lithosphere and followed by a thermal post breakup re-equilibration (Fig. 7). We assumed a thinning factor of 4 (meaning a crustal thickness of 7.5 km for an initial crustal thickness of 30 km) which is in agreement with the observed crustal thinning at ridge A (Fig. 2). In this case, pre-rift heat-flow is set at 60 $mW.m^{-2}$ corresponding to the average worldwide continental value (McKenzie, 1978). During the rifting phase of the SCS (40-30 Ma) the heat-flow increases up to 275 $mW.m^{-2}$ and decreases exponentially to the current value of 110 $mW.m^{-2}$ (Fig. 7c). This thermal evolution provides a thermal maturity curve very similar to the constant heat-flow model (Fig. 6) ,although, the obtained thermal maturity is slightly higher in the early post-rift sequence, compared to the previous model. These differences are small and cannot explain the high maturity values below Tg at Site U1499 (Fig. 6).

The third model includes the presence of an erosional event prior to the Cenozoic rifting with a constant heat-flow through time, using the present-day value (Fig. 6). In such scenario, the gravel unit of the Site U1499 is assumed to be pre-rift in age. A pre-rift erosional phase (pre-Tg) has been seismically reported and locally drilled in many localities across the SCS margins (Larsen et al., 2018a; Liang et al., 2019). The post-rift thermal maturity is alike the first model and the occurrence of 2.2 km of erosion before the Cenozoic rifting allows a fit to maturity values in the gravel unit, e.g. it predicts vitrinite reflectance values of about 1.22 Ro% at 995

mbsf and 1014 mbsf (Fig. 4). Nevertheless, the modelled curve is not able to fit the deeper thermal maturity values around 1.7-1.8 Ro%.

Neither present day basal heat-flow, heating during prior episodes of burial nor heating due to lithospheric-thinning can supply sufficient heat to explain the gradient in thermal maturity measured in the gravel unit at the base of U1499. However, volcanism and related thermal effects have occurred at site U1502 in the form of hydrothermally altered MORB. It is thus geologically reasonable to investigate whether heating due to the presence of a magmatic body from which the MORB formed may explain the high thermal maturity in the pre-/syn-rift succession of U1499.

To test if the high thermal maturity gradient recorded in the gravel unit can be recreated by heating within the aureole of a magmatic body we combined the results of the Basinmod 2D software with predictions made by the SILLi 1.0 software (Iyer et al., 2018). The SILLi software is designed to predict the effect of magmatic sills on the thermal maturity of a stratigraphic succession. In this case we assume that beneath the pre-/syn-rift gravel unit or nearby is a magmatic body. The intrusion was assumed to have been emplaced during the early Oligocene, during breakup. A set of models was performed to test the depth and size of the intrusion that could best recreate measured thermal maturities. The best fit was obtained by a body 200 m thick located at 1150 mbsf (or 70 m beneath the TD of hole U1499B). Sensitivity tests are provided in Supplement (SI-6). It is worth noting that this solution is not unique and different sizes, depths and numbers of intrusion could also fit measured data.

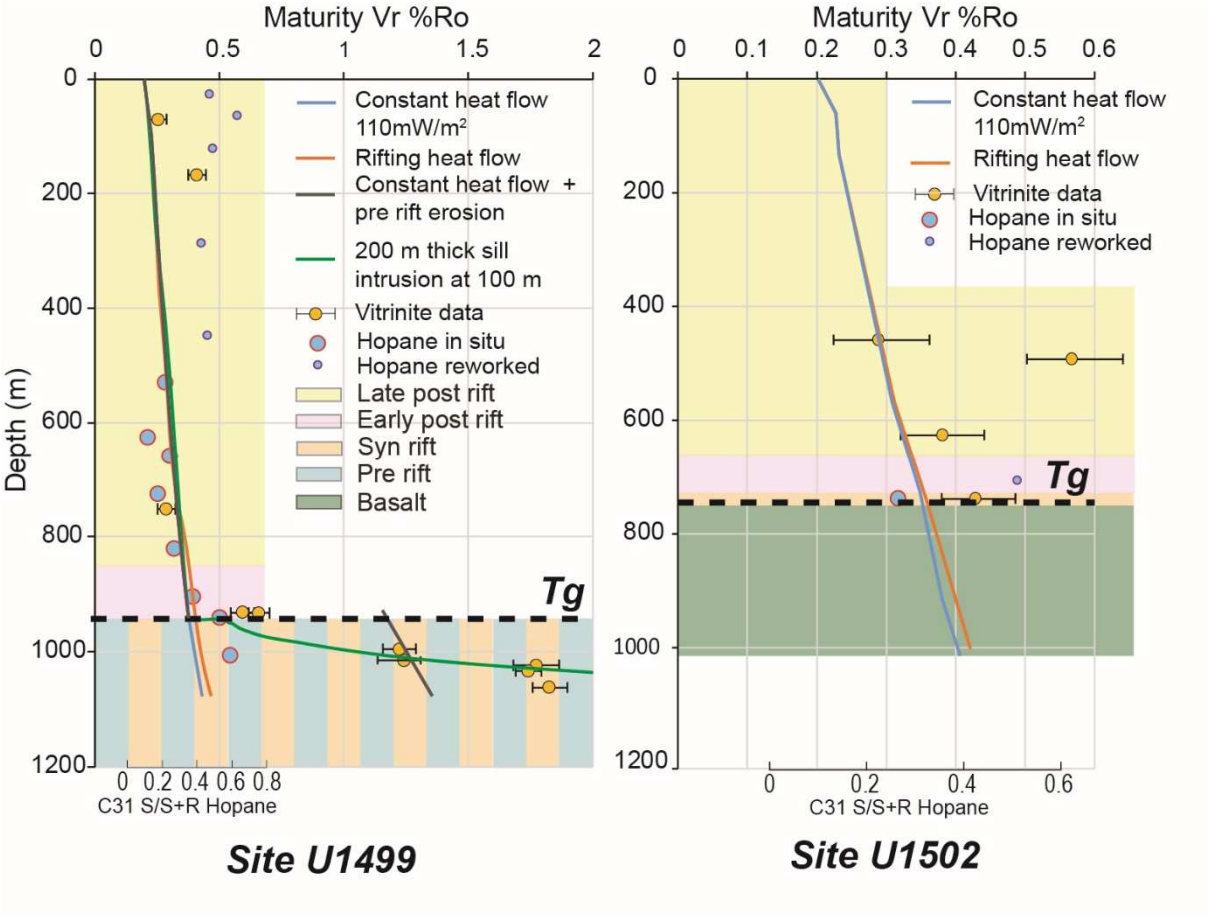

Fig. 6 1D thermal models for site U1499 and U1502, with the 4 investigated scenarios: 1) constant heat-flow 110 mW.m^{-2}. 2) McKenzie type model, heat-flow for a thinning factor of 4 (i.e. pre rift heat-flow at 60 mW.m^{-2}, a rift phase from 40-30 Ma increases the heat-flow to 275 mW.m^{-2} followed by an exponential decrease to the current value of 110 mW.m^{-2}). 3) constant heat-flow with erosion. 4) The pre-Tg thermal maturity is modelled following the software SILLi. 1.0 assuming the emplacement of 200 m thick Sill intrusion at 100 m during the early Oligocene. The post-Tg thermal maturity is modelled following the scenario 1.

7.Discussion

7.1 Tectonic and thermal evolution of the SE China COT

We analysed the thermal maturity of the sedimentary record on the most distal thinned continental crust of the SE China rifted margin to assess the thermal effect of rifting and breakup processes. The tectonic and thermal evolution observed at ridge A are summarised in Figure 7.

An extreme thinning of the Eocene continental lithosphere is recorded at Ridge A. This thinned crust is directly juxtaposed to the MORB-type volcanic rocks found at Ridges B and C, which correspond to the onset of seafloor spreading at 30 Ma (Larsen et al., 2018a). The gravel unit at Site U1499 is either an initial coarse syn-rift sedimentary infill or older pre-rift sediment. Due to limited burial (less than 500 m), thermal effects of crustal thinning are not well recorded in the sediment-fill deposited at the earliest stages of rifting, despite the expectation that heat-flow would have increased during lithospheric-thinning (McKenzie, 1978) (Fig .7).

During the latest stages of rifting, MORB type volcanism may have had a surface expression as is the case for the basalts found at U1502, but it should also be noted that such magmatism can also thermally alter older sediment-fill as is seen in the pre-/syn-rift sediments at U1499. Mechanistically this would be done by magma intruding into sediments during late syn-rift stages; an intrusion would rapidly increase temperature for a geologically short duration, by locally increasing heat flow and thermally altering sediment within contact aureoles (Fig. 7 Fjeldskaar et al., 2008; Muirhead et al., 2017; Peace et al., 2017).

At Site U1502, volcanic rocks and a short 10 m interval of the overlying sediments are hydrothermally altered, but alteration is absent in the overlying 720 m of post-rift sequence. It is important to note that the deepest thermal maturity measurement at site U1502 is indeed higher than might be expected for its depth (with less than 750 m of burial thermal maturity at U1502 equals that found at 2 km in other sedimentary basins e.g. Farrimond et al. 1998). But despite the evidence of an active hydrothermal system, the thermal alteration evidenced in both vitrinite reflectance and biomarker data was explained by burial metamorphism with a heat flow of 275-110 $mW.m^{-2}$ (Fig. 6). Thus it seems that hydrothermal fluids have probably

not affected the organic matter at U1502, at least not directly. Hydrothermal fluids can certainly alter thermal maturity at both spreading centres (Simoneit et al. 1984), and in back arc basins (Bowden et al. 2016). But it is commonly acknowledged that short lived fluid pulses may not alter sedimentary organic matter if not sustained for sufficient duration (Parnell 2010). Thus an interpretation of the presence of hydrothermal mineral phases indicating temperatures greater than 200 °C (Larsen et al 2018), but without alteration of sedimentary organic matter, would be that hydrothermal activity is less efficient at transferring additional heat to sediments than magmatism in the SE China COT. This may reflect the hydrothermal system at U1502 operating for only a short time, or the hydrothermal system waning significantly by the time overlying sediment was deposited.

In the earliest post-rift gravels of Site U1499 (~5m of matrix supported breccia), thermal maturity is less than the deepest gravel unit (0.59-0.66 Ro% cf. 1.6-1.8 Ro%), and is only slightly more than would be predicted by a constant heat-flow model (Fig. 6). We offer two explanations for this observation. First, magmatic activity and associated thermal effects may have continued for a few million years after breakup, and subsequently waning magmatic activity changed thermal maturity (Fig.7). A second explanation is that a true *in-situ* thermal maturity was not measured, and that our vitrinite and Raman data are strongly biased towards organic matter reworked from the underlying gravel unit. The effect of magmatism on the thermal maturity of the SE China COT is clear, however, the emplacement of this breakup related magmatism was likely spatially heterogeneously distributed across the COT causing important variations within the thermal maturity of the pre- and syn-rift and potentially earliest post-rift sediments.

Soon after the phases of extensional break-up and localisation of magmatism at spreading ridges the SE China COT passively subsided. The post-rift succession has a low thermal maturity and is in the immature stages of hydrocarbon generation at sites U1499 and U1502. The thermal maturities of the post-rift successions at these two sites can be explained by basal heat flows that are constant over time or match a McKenzie-type thermal evolution (Fig. 6). The lack of differentiation between the two models of heat flow maybe due to limited burial and a low early post-rift sedimentation rate (~8-10 $mm.yr^{-1}$). From 30 to 11 Ma, less than 100 m thickness of early post-rift sediments was deposited. This lack of burial prevents significant differences in thermal maturity developing between the McKenzie type and constant heat-flow models, as they differ mostly during rifting and early post-rift times. The late post-rift sequence is thicker, but after 20 Ma the heat-flow had already reduced significantly compared to the breakup phases (Fig.7).

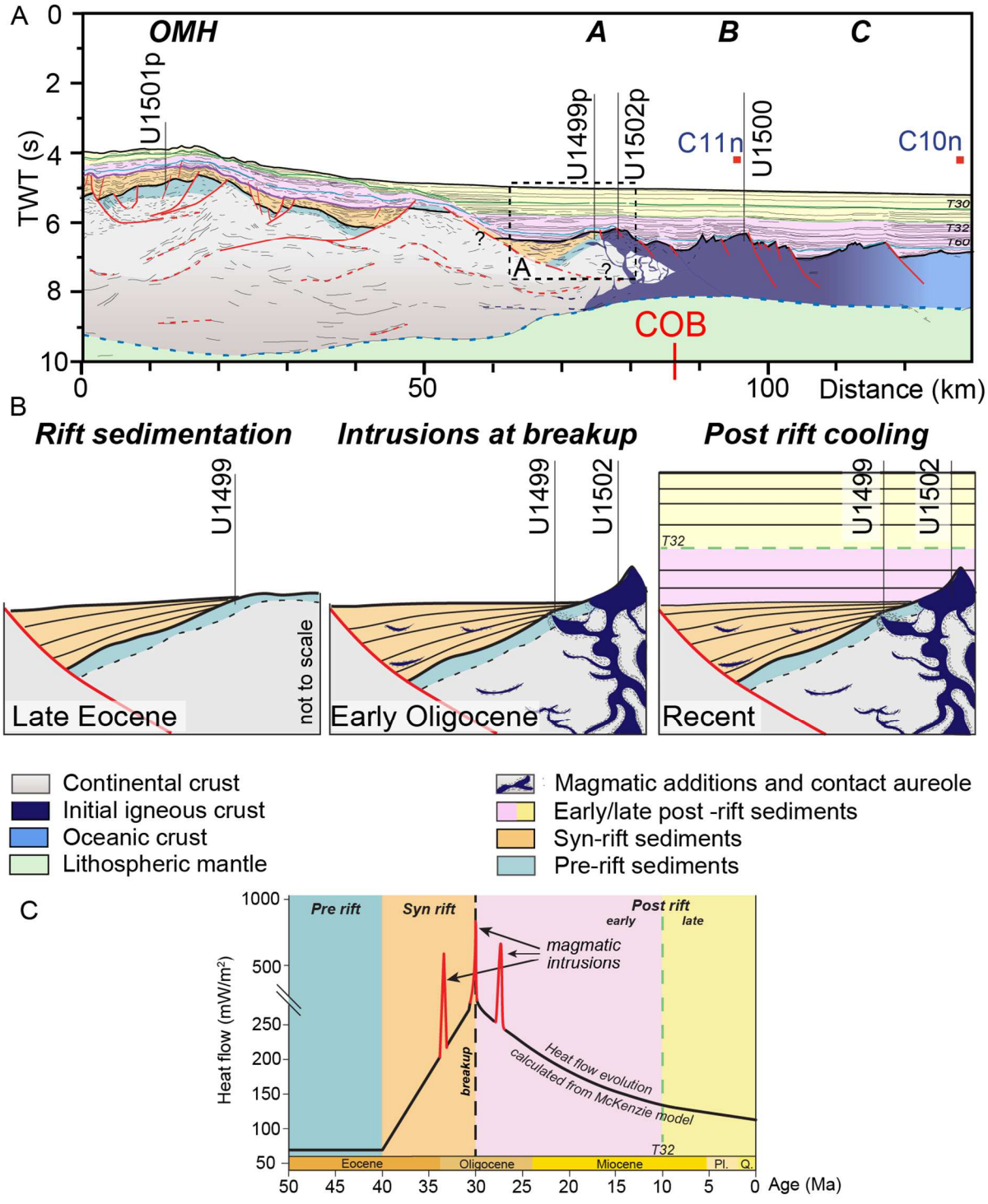

522

523 **Fig. 7** A) Seismic interpretation of the SE China COT with the location of the COB determined
524 by gravity modelling (Nirrengarten et al., subm); B) Schematic evolution of ridge A, the
525 breakup related magmatic additions increase the thermal maturity in heterogeneously
526 distributed contact aureoles, early post-rift sedimentation rate is low related to an
527 insufficient burial to record the breakup thermal peak in the thermal maturity data. C)
528 Schematic evolution of heat-flow showing the background McKenzie rift type evolution and
529 the effect of punctual magmatic additions.

7.2 Factors controlling thermal evolution and maturity of sediments at COT

Late syn-rift magmatism plays a prominent role in the thermal evolution of the SE-China COT. However, parameters controlling the thermal evolution and thermal maturity of sedimentary succession at COT are multiple and present complex interplays in time and space as exemplified in previous works and summarized in Figure 8. In this section, we aim to provide an overview of the main factors favouring a regime of high heat-flows and temperatures in distal rifted margins and how they are recorded in sedimentary successions.

The thinning of the continental lithosphere, and the associated rise of the asthenosphere that compresses the isotherms and subsequently increases the geothermal gradient, is a major factor in regional thermal evolution (McKenzie, 1978) (Fig.7). Different modes of lithospheric thinning (e.g. simple-shear, pure-shear, depth dependent thinning) variably affect heat-flows and their spatial distribution as well as their evolution during and after extension (Buck et al., 1988; Driscoll and Karner, 1998; Kusznir and Karner, 2007). In the case of the SCS, heat-flow measurements suggest a pure-shear mode of extension (Nissen et al., 1995). However, in the segment of the SE-China margin that we investigated, the effect of late syn-rift magmatism and the limited number of wells precludes any unambiguous determination of the thinning mode based on thermal data.

Radiogenic heat production from residual continental crust represents another parameter with the potential to influence thermal evolution at rifted margins. This parameter is variable depending on the pre-rift history and the composition of continental crustal rocks (Jaupart and Mareschal, 2015). Radiogenic heating has been shown to be caused by Mesozoic granitic batholiths that are present across the SCS (Savva et al., 2014), and may locally contribute to heat-flow, and may be partly responsible for high heat-flows in the region (110 $mW.m^{-2}$).

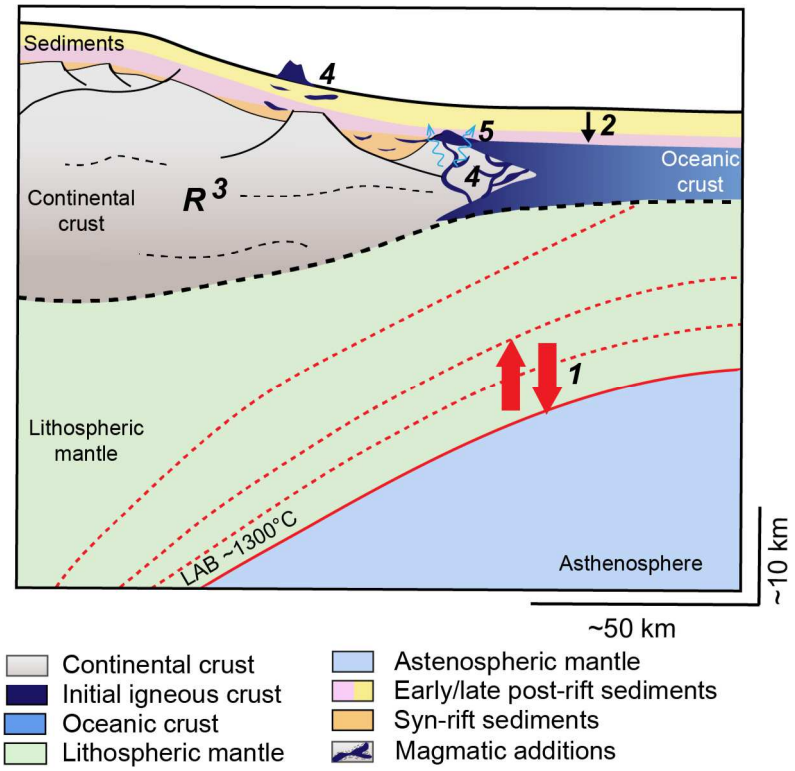

553

554 **Fig. 8:** Schematic cross-section of a COT illustration the main parameters acting on the thermal
555 evolution and its record in the sedimentary section. 1) Thinning mode of the continental lithosphere
556 controlling the rise of isotherms and the progressive post-breakup cooling; 2) Sedimentary burial; 3)
557 R: Radiogenic heat production of the residual thinned continental crust; 4) Syn-rift or post-rift
558 magmatic intrusions and there contact alteration aureoles; 5) Hydrothermal fluid circulations. LAB:
559 Lithosphere Asthenosphere Boundary

560

561 Rifting and eventually breakup may induce additional heating through various heat-transfer
562 mechanisms, all of which could locally increase thermal maturity. In this case, a modelled syn-
563 rift magmatic intrusion increases the thermal maturity of the lowermost sedimentary
564 succession at Site U1499 sufficiently to explain observed thermal maturation. The effect of an
565 isolated magmatic intrusion is limited and only affects the surrounding sediments of
566 approximately 1,5-2 times the width of the intrusion (Fjeldskaar et al., 2008). However if
567 several magmatic sills are emplaced across a sedimentary succession, which is probable, this
568 additional heat may significantly influence thermal maturity across a sedimentary basin as
569 seen in the Rockall Trough (Fjeldskaar et al., 2008; Muirhead et al., 2017). Magmatism is often

570 related to hydrothermal fluids, which play an important role in the COT by enabling the
571 transfer of elements and heat between the mantle and superficial sediments (Pinto et al.,
572 2015). However, as exemplified at Site U1502, hydrothermal activity needs to be sustained
573 over time in order for organic matter to be significantly altered (Parnell, 2010). In the case of
574 mantle exhumation in the COT of regions such as the West Iberian or the fossil Alpine margins,
575 the serpentinization process may contribute to elevating or maintaining high-flow conditions
576 during late-syn-rift or early post-rift stages (Callies et al., 2018).

577 Syn- and early post-rift sedimentation rates and therefore burial are crucial to recording the
578 high heat flow conditions during early post-rift phases. In contrast to the SE-China COT, the
579 Pyrenean fossil hyper-extended rift basin is characterized by pre-rift evaporites, massive syn-
580 rift and early post-rift sedimentation, that blanket and bury sediment leading to the recording
581 of high thermal maturities in organic matter (Clerc and Lagabrielle, 2014). Without significant
582 burial (~3-6 km in the Pyrenean case study (Clerc and Lagabrielle, 2014)), the temperature at
583 the base of a sedimentary succession would never be great enough even were a geothermal
584 gradient high (> 80°C.km^{-1}).

585 Late post-rift magmatism is not indicated by our dataset while it is inferred in other localities
586 of the SE China margin and clearly mapped in the oceanic domain of the SCS as shown by
587 occurrence of several seamounts (Sibuet et al., 2016). Post-rift volcanism at a COT modifies
588 the thermal regime in a way similar to that seen in the high local heat-flows in places such as
589 the Gulf of Aden (Lucazeau et al., 2009). Such post-rift anomalous high heat flows alter the
590 thermal maturity acquired during burial and cooling of the rifted margin. Elevated post-rift
591 heat-flows have also been related to small-scale convection cells, formed by the difference in
592 temperature difference between continental and oceanic lithosphere (Lucazeau et al., 2008).

593 The operation of such convection cells for either a limited time-period or a very long time-
594 period is not well constrained but may have a major impact on the COT thermal evolution and
595 therefore on the thermal maturity of associated sedimentary basins.

596 **8.Conclusion**

597 Despite progress in our understanding of the formation of rifted margins, the thermal
598 evolution of COT remains a matter of debate. IODP expeditions 367-368 provided an
599 opportunity to sample and model the thermal evolution on the thinnest continental crust of
600 the SE China margin represented by Ridge A. The last fragment of the residual continental
601 crust drilled by these expeditions is directly juxtaposed against the oldest oceanic crust and
602 has been sampled by two drilling sites U1499 and U1502. Based on vitrinite reflectance,
603 Raman spectroscopy and biomarker analysis, rapid changes in thermal maturity with depth
604 are observed at Site U1499 in the oldest rift sediments. Present day heat-flows and heat-flow
605 modelled according to a McKenzie-type rifting environment could not explain measurements
606 of thermal maturity in the deepest sediments encountered. The heat-flow needed to recreate
607 the high thermal maturity in the deepest section can only realistically be explained by syn-rift
608 magmatism, notably encountered at the adjacent Site U1502. While of high thermal maturity
609 for its shallow depth of burial, the early post-rift succession of U1499 and U1502 is notably
610 less thermally mature.

611 Ultimately, the thermal evolution of COTs results from the interactions of several different
612 parameters that challenge the current understanding of such domains. Beside the regional
613 effect of lithospheric thinning, local thermal perturbations generated by magmatic additions
614 during and after extension, as well as poorly constrained deep thermal anomalies during post-
615 rift phases, may significantly affect the local thermal evolution of a COT.

References

Amante, C., Eakins, B.W., 2009. ETOPO1 1 Arc-Minute Global Relief Model: Procedures, Data Sources and Analysis. https://doi.org/10.7289/V5C8276M

Amo, M., Suzuki, N., Shinoda, T., Ratnayake, N.P., Takahashi, K., 2007. Diagenesis and distribution of sterenes in Late Miocene to Pliocene marine siliceous rocks from Horonobe (Hokkaido, Japan). Org. Geochem. 38, 1132–1145. https://doi.org/10.1016/j.orggeochem.2007.02.010

Beyssac, O., Goffé, B., Chopin, C., Rouzaud, J.N., 2002. Raman spectra of carbonaceous material in metasediments: A new geothermometer. J. Metamorph. Geol. 20, 859–871. https://doi.org/10.1046/j.1525-1314.2002.00408.x

Bowden, S.A., Walker, J., Ziolkowski, M., and Taylor, C., 2016. Data report: bitumen extracted from hydrothermally altered sediments encountered during Expedition 331. In Takai, K., Mottl, M.J., Nielsen, S.H., and the Expedition 331 Scientists, Proceedings of the Integrated Ocean Drilling Program, 331: Tokyo (Integrated Ocean Drilling Program Management International, Inc.). doi:10.2204/iodp.proc.331.201.2016

Briais, A., Patriat, P., Tapponnier, P., 1993. Updated interpretation of magnetic anomalies and seafloor spreading stages in the south China Sea: Implications for the Tertiary tectonics of Southeast Asia. J. Geophys. Res. Solid Earth 98, 6299–6328. https://doi.org/10.1029/92JB02280

Buck, W.R., Martinez, F., Steckler, M.S., Cochran, J.R., 1988. Thermal consequences of lithospheric extension:pure and simple. Tectonics 7, 213–234.

Callies, M., Filleaudeau, P.Y., Dubille, M., Lorant, F., 2018. How to predict thermal stress in hyperextended margins: Application of a new lithospheric model on the Iberia margin. Am. Assoc. Pet. Geol. Bull. 102, 545–547. https://doi.org/10.1306/07111716116

Clerc, C., Lagabrielle, Y., 2014. Thermal control on the modes of crustal thinning leading to mantle exhumation: Insights from the cretaceous pyrenean hot paleomargins. Tectonics 33, 1340–1359. https://doi.org/10.1002/2013TC003471

Driscoll, N.W., Karner, G.D., 1998. Lower crustal extension across the Northern Carnarvon basin, Australia: Evidence for an eastward dipping detachment. J. Geophys. Res. Solid Earth 103, 4975–4991. https://doi.org/10.1029/97JB03295

Farrimond, P., Taylor, A., TelnÆs, N., 1998. Biomarker maturity parameters: the role of generation and thermal degradation. Org. Geochem. 29, 1181–1197. https://doi.org/10.1016/S0146-6380(98)00079-5

Fjeldskaar, W., Helset, H.M., Johansen, H., Grunnaleite, I., Horstad, I., 2008. Thermal modelling of magmatic intrusions in the Gjallar Ridge, Norwegian Sea: implications for vitrinite reflectance and hydrocarbon maturation. Basin Res. 20, 143–159. https://doi.org/10.1111/j.1365-2117.2007.00347.x

654 Franke, D., Savva, D., Pubellier, M., Steuer, S., Mouly, B., Auxietre, J.-L., Meresse, F., Chamot-
655 Rooke, N., 2014. The final rifting evolution in the South China Sea. Mar. Pet. Geol. 58,
656 704–720. https://doi.org/10.1016/j.marpetgeo.2013.11.020

657 Gardiner, D., Schofield, N., Finlay, A., Mark, N., Holt, L., Grove, C., Forster, C., Moore, J.,
658 2019. Modeling petroleum expulsion in sedimentary basins: The importance of igneous
659 intrusion timing and basement composition. Geology 47, 1–5.
660 https://doi.org/10.1130/G46578.1

661 Iyer, K., Svensen, H., Schmid, D.W., 2018. SILLi 1.0: A 1-D numerical tool quantifying the
662 thermal effects of sill intrusions. Geosci. Model Dev. 11, 43–60.
663 https://doi.org/10.5194/gmd-11-43-2018

664 Jagoutz, O., Müntener, O., Manatschal, G., Rubatto, D., Péron-Pinvidic, G., Turrin, B.D., Villa,
665 I.M., 2007. The rift-to-drift transition in the North Altantic: A stuttering start of the
666 MORB machine? Geology 35, 1087–1090. https://doi.org/10.1130/G23613A.1

667 Jaupart, C., Mareschal, J.C., 2015. Heat Flow and Thermal Structure of the Lithosphere,
668 Treatise on Geophysics: Second Edition. Elsevier B.V. https://doi.org/10.1016/B978-0-
669 444-53802-4.00114-7

670 Kusznir, N.J., Karner, G.D., 2007. Continental lithospheric thinning and breakup in response
671 to upwelling divergent mantle flow: application to the Woodlark, Newfoundland and
672 Iberia margins. Geol. Soc. London, Spec. Publ. 282, 389–419.
673 https://doi.org/10.1144/SP282.16

674 Lahfid, A., Beyssac, O., Deville, E., Negro, F., Chopin, C., Goffé, B., 2010. Evolution of the
675 Raman spectrum of carbonaceous material in low-grade metasediments of the Glarus
676 Alps (Switzerland). Terra Nov. 22, 354–360. https://doi.org/10.1111/j.1365-
677 3121.2010.00956.x

678 Larsen, H. C., Mohn, G., Nirrengarten, M., Sun, Z., Stock, J., Jian, Z., Klaus, A., Alvarez-
679 Zarikian, C.A., Boaga, J., Bowden, S.A., Briais, A., Chen, Y., Cukur, D., Dadd, K., Ding, W.,
680 Dorais, M., Ferré, E.C., Ferreira, F., Furusawa, A., Gewecke, A., Hinojosa, J., Höfig, T.W.,
681 Hsiung, K.H., Huang, B., Huang, E., Huang, X.L., Jiang, S., Jin, H., Johnson, B.G.,
682 Kurzawski, R.M., Lei, C., Li, B., Li, L., Li, Y., Lin, J., Liu, C., Liu, C., Liu, Z., Luna, A.J., Lupi, C.,
683 McCarthy, A., Ningthoujam, L., Osono, N., Peate, D.W., Persaud, P., Qiu, N., Robinson,
684 C., Satolli, S., Sauermilch, I., Schindlbeck, J.C., Skinner, S., Straub, S., Su, X., Su, C., Tian,
685 L., van der Zwan, F.M., Wan, S., Wu, H., Xiang, R., Yadav, R., Yi, L., Yu, P.S., Zhang, C.,
686 Zhang, J., Zhang, Y., Zhao, N., Zhong, G., Zhong, L., 2018a. Rapid transition from
687 continental breakup to igneous oceanic crust in the South China Sea. Nat. Geosci. 11,
688 782–789. https://doi.org/10.1038/s41561-018-0198-1

689 Larsen, H.C., Sun, Z., Stock, J.M., Jian, Z., Alvarez Zarikian, C.A., Klaus, A., Boaga, J., Bowden,
690 S.A., Briais, A., Chen, Y., Cukur, D., Dadd, K.A., Ding, W., Dorais, M.J., Ferré, E.C.,
691 Ferreira, F., Furusawa, A., Gewecke, A.J., Hinojosa, J.L., Höfig, T.W., Hsiung, K.H., Huang,
692 B., Huang, E., Huang, X.L., Jiang, S., Jin, H., Johnson, B.G., Kurzawski, R.M., Lei, C., Li, B.,
693 Li, L., Li, Y., Lin, J., Liu, C., Liu, C., Liu, Z., Luna, A., Lupi, C., McCarthy, A.J., Mohn, G.,
694 Ningthoujam, L.S., Nirrengarten, M., Osono, N., Peate, D.W., Persaud, P., Qiu, N.,
695 Robinson, C.M., Satolli, S., Sauermilch, I., Schindlbeck, J.C., Skinner, S.M., Straub, S.M.,
696 Su, X., Tian, L., van der Zwan, F.M., Wan, S., Wu, H., Xiang, R., Yadav, R., Yi, L., Zhang, C.,

Zhang, J., Zhang, Y., Zhao, N., Zhong, G., Zhong, L., 2018b. Expedition 367/368 summary, in: Proceedings of the International Ocean Discovery Program Volume 367/368. https://doi.org/10.14379/iodp.proc.367368.101.2018

Larsen, H.C., Jian, Z., Alvarez Zarikian, C.A., Sun, Z., Stock, J.M., Klaus, A., Boaga, J., Bowden, S.A., Briais, A., Chen, Y., Cukur, D., Dadd, K.A., Ding, W., Dorais, M.J., Ferré, E.C., Ferreira, F., Furusawa, A., Gewecke, A.J., Hinojosa, J.L., Höfig, T.W., Hsiung, K.H., Huang, B., Huang, E., Huang, X.L., Jiang, S., Jin, H., Johnson, B.G., Kurzawski, R.M., Lei, C., Li, B., Li, L., Li, Y., Lin, J., Liu, C., Liu, C., Liu, Z., Luna, A., Lupi, C., McCarthy, A.J., Mohn, G., Ningthoujam, L.S., Nirrengarten, M., Osono, N., Peate, D.W., Persaud, P., Qiu, N., Robinson, C.M., Satolli, S., Sauermilch, I., Schindlbeck, J.C., Skinner, S.M., Straub, S.M., Su, X., Tian, L., van der Zwan, F.M., Wan, S., Wu, H., Xiang, R., Yadav, R., Yi, L., Zhang, C., Zhang, J., Zhang, Y., Zhao, N., Zhong, G., Zhong, L., 2018c. Site U1502, in: Proceedings of the International Ocean Discovery Program Volume 367/368. https://doi.org/10.14379/iodp.proc.367368.106.2018

Lescoutre, R., Tugend, J., Brune, S., Masini, E., Manatschal, G., 2019. Thermal Evolution of Asymmetric Hyperextended Magma-Poor Rift Systems: Results From Numerical Modeling and Pyrenean Field Observations. Geochemistry, Geophys. Geosystems 2019GC008600. https://doi.org/10.1029/2019GC008600

Liang, Y., Delescluse, M., Qiu, Y., Pubellier, M., Chamot-Rooke, N., Wang, J., Nie, X., Watremez, L., Chang, S., Pichot, T., Savva, D., Meresse, F., 2019. Décollements, detachments and rafts in the extended crust of Dangerous Ground, South China Sea: the role of inherited contacts. Tectonics 2018TC005418. https://doi.org/10.1029/2018TC005418

Lucazeau, F., Leroy, S., Autin, J., Bonneville, A., Goutorbe, B., Watremez, L., D'acremont, E., Düsünur, D., Rolandone, F., Huchon, P., Bellahsen, N., Tuchais, P., 2009. Post-rift volcanism and high heat-flow at the ocean-continent transition of the eastern Gulf of Aden. Terra Nov. 21, 285–292. https://doi.org/10.1111/j.1365-3121.2009.00883.x

Lucazeau, F., Leroy, S., Bonneville, A., Goutorbe, B., Rolandone, F., D'Acremont, E., Watremez, L., Düsünur, D., Tuchais, P., Huchon, P., Bellahsen, N., Al-Toubi, K., 2008. Persistent thermal activity at the eastern gulf of Aden after continental break-up. Nat. Geosci. 1, 854–858. https://doi.org/10.1038/ngeo359

Lünsdorf, N.K., Lünsdorf, J.O., 2016. Evaluating Raman spectra of carbonaceous matter by automated, iterative curve-fitting. Int. J. Coal Geol. 160–161, 51–62. https://doi.org/10.1016/j.coal.2016.04.008

Machel, H.G., 2004. Concepts and models of dolomitization: a critical reappraisal. Geol. Soc. London, Spec. Publ. 235, 7–63. https://doi.org/10.1144/GSL.SP.2004.235.01.02

Mackenzie, A.S., McKenzie, D., 1983. Isomerization and aromatization of hydrocarbons in sedimentary basins formed by extension. Geol. Mag. 120, 417–470. https://doi.org/10.1017/S0016756800027461

Manatschal, G., 2004. New models for evolution of magma-poor rifted margins based on a review of data and concepts from West Iberia and the Alps. Int. J. Earth Sci. 93, 432–466. https://doi.org/10.1007/s00531-004-0394-7

McKenzie, D., 1978. Some remarks on the formation of sedimentary basins. Earth Planet. Sci. Lett. 40, 25–32.

Muirhead, D.K., Bowden, S.A., Parnell, J., Schofield, N., 2017. Source rock maturation owing to igneous intrusion in rifted margin petroleum systems. J. Geol. Soc. London. 174, 979–987. https://doi.org/10.1144/jgs2017-011

Nirrengarten M., Mohn G., Kusznir N. J., Sapin F., Despinois F., Pubellier M., Chang S. P., Larsen H. C., Ringenbach J. C., Extension modes and breakup processes of the Southeast China-Northwest Palawan conjugate rifted margins, . Mar. Pet. Geol in press

Nissen, S.S., Hayes, D.E., Bochu, Y., Zeng, W., Chen, Y., Nu, X., 1995. Gravity, heat flow, and seismic constraints on the processes of crustal extension: Northern margin of the South China Sea. J. Geophys. Res. 100, 22447. https://doi.org/10.1029/95JB01868

Parnell, J., 2010. Potential of palaeofluid analysis for understanding oil charge history. Geofluids 73–82. https://doi.org/10.1111/j.1468-8123.2009.00268.x

Peace, A., McCaffrey, K., Imber, J., Hobbs, R., van Hunen, J., Gerdes, K., 2017. Quantifying the influence of sill intrusion on the thermal evolution of organic-rich sedimentary rocks in nonvolcanic passive margins: an example from ODP 210-1276, offshore Newfoundland, Canada. Basin Res. 29, 249–265. https://doi.org/10.1111/bre.12131

Peters, K.E., Nelson, P.H., 2012. Criteria to determine borehole formation temperatures for calibration of basin models. SEPM Spec. Publ. 5–15.

Pinto, V.H.G., Manatschal, G., Karpoff, A.M., Viana, A., 2015. Tracing mantle-reacted fluids in magma-poor rifted margins: The example of Alpine Tethyan rifted margins. Geochemistry, Geophys. Geosystems 16, 3271–3308. https://doi.org/10.1002/2015GC005830

Pross, J., Pletsch, T., Shillington, D.J., Ligouis, B., Schellenberg, F., Kus, J., 2007. Thermal alteration of terrestrial palynomorphs in mid-Cretaceous organic-rich mudstones intruded by an igneous sill (Newfoundland Margin, ODP Hole 1276A). Int. J. Coal Geol. 70, 277–291. https://doi.org/10.1016/j.coal.2006.06.005

Royden, L., Sclater, J.G., von Herzen, R.P., 1980. Continental margin subsidence and heat flow: important parameters in formation of petroleum hydrocarbons. Am. Assoc. Pet. Geol. Bull. 64, 173–187. https://doi.org/10.1306/2F91894B-16CE-11D7-8645000102C1865D

Savva, D., Pubellier, M., Franke, D., Chamot-Rooke, N., Meresse, F., Steuer, S., Auxietre, J.L., 2014. Different expressions of rifting on the South China Sea margins. Mar. Pet. Geol. 58, 579–598. https://doi.org/10.1016/j.marpetgeo.2014.05.023

Schito, A., Corrado, S., 2018. An automatic approach for characterization of the thermal maturity of dispersed organic matter Raman spectra at low diagenetic stages. Geol. Soc. London, Spec. Publ. SP484.5. https://doi.org/10.1144/sp484.5

Schito, A., Romano, C., Corrado, S., Grigo, D., Poe, B., Scienze, D., Geologiche, S., Roma, S., Murialdo, L.S.L., Spa, E., Division, P., Emilia, V., Milanese, S.D., 2017. Organic Geochemistry Diagenetic thermal evolution of organic matter by Raman spectroscopy. Org. Geochem. 106, 57–67. https://doi.org/10.1016/j.orggeochem.2016.12.006

780 Schmidt Mumm, A., Inan, S., 2016. Microscale organic maturity determination of graptolites
781 using Raman spectroscopy. Int. J. Coal Geol. 162, 96–107.
782 https://doi.org/10.1016/j.coal.2016.05.002

783 Sclater, J.G., Jaupart, C., Galson, D., 1980. The heat flow through oceanic and continental
784 crust and the heat loss of the Earth. Rev. Geophys. 18, 269–311.
785 https://doi.org/10.1029/RG018i001p00269

786 Sibuet, J.C., Yeh, Y.C., Lee, C.S., 2016. Geodynamics of the South China Sea. Tectonophysics
787 692, 98–119. https://doi.org/10.1016/j.tecto.2016.02.022

788 Simoneit, B.R.T., Philp, R.P., Jenden, P.D., and Galimov, E.M., 1984. Organic geochemistry of
789 Deep Sea Drilling Project sediments from the Gulf of California–hydrothermal effects on
790 unconsolidated diatom ooze. Organic Geochemistry, 7(3–4):173–205.
791 http://dx.doi.org/10.1016/0146-6380(84)90115-3

792 Suárez-Ruiz, I., Flores, D., Mendonça Filho, J.G., Hackley, P.C., 2012. Review and update of
793 the applications of organic petrology: Part 1, geological applications. Int. J. Coal Geol.
794 99, 54–112. https://doi.org/10.1016/j.coal.2012.02.004

795 Sun, Z., Stock, J.M., Klaus, A., Larsen, H.C., Jian, Z., Alvarez Zarikian, C.A., Boaga, J., Bowden,
796 S.A., Briais, A., Chen, Y., Cukur, D., Dadd, K.A., Ding, W., Dorais, M.J., Ferré, E.C.,
797 Ferreira, F., Furusawa, A., Gewecke, A.J., Hinojosa, J.L., Höfig, T.W., Hsiung, K.H., Huang,
798 B., Huang, E., Huang, X.L., Jiang, S., Jin, H., Johnson, B.G., Kurzawski, R.M., Lei, C., Li, B.,
799 Li, L., Li, Y., Lin, J., Liu, C., Liu, C., Liu, Z., Luna, A., Lupi, C., McCarthy, A.J., Mohn, G.,
800 Ningthoujam, L.S., Nirrengarten, M., Osono, N., Peate, D.W., Persaud, P., Qiu, N.,
801 Robinson, C.M., Satolli, S., Sauermilch, I., Schindlbeck, J.C., Skinner, S.M., Straub, S.M.,
802 Su, X., Tian, L., van der Zwan, F.M., Wan, S., Wu, H., Xiang, R., Yadav, R., Yi, L., Zhang, C.,
803 Zhang, J., Zhang, Y., Zhao, N., Zhong, G., Zhong, L., 2018. Site U1499, in: Proceedings of
804 the International Ocean Discovery Program Volume 367/368.
805 https://doi.org/10.14379/iodp.proc.367368.103.2018

806 Taylor, B., Hayes, DE, 1983. Origin and history of the South China Sea basin, in: Hayes, Dennis
807 (Ed.), The Tectonic and Geologic Evolution of Southeast Asian Seas and Islands: Part 2.
808 pp. 23–56.

809 Tissot, B., Espitalié, J., 1975. L'evolution thermique de la matière organique des sédiments :
810 applications d'une simulation mathématique. Potentiel pétrolier des bassins
811 sédimentaires de reconstitution de l'histoire thermique des sédiments. Rev. l'Institut
812 Français du Pétrole 30, 743–778. https://doi.org/10.2516/ogst:1975026

813 Wilkins, R.W.T., Boudou, R., Sherwood, N., Xiao, X., 2014. Thermal maturity evaluation from
814 inertinites by Raman spectroscopy: The "RaMM" technique. Int. J. Coal Geol. 128–129,
815 143–152. https://doi.org/10.1016/j.coal.2014.03.006

816 Zhou, D., Ru, K., Chen, H., 1995. Kinematics of Cenozoic extension on the South China Sea
817 continental margin and its implications for the tectonic evolution of the region.
818 Tectonophysics 251, 161–177. https://doi.org/10.1016/0040-1951(95)00018-6

Acknowledgments

This research used data provided by the International Ocean Discovery Program (IODP).We thanks the participants to IODP Expedition 367-368 as well as the captains and crew of the Joides Resolution. Seismic sections originate from the IODP Expedition 367/368/368X proceeding volume. Platte River Associates, Inc is thanked for providing an academic licence of BasinMod 2D. We acknowledge IODP France and ECORD for the support. Funding for this research was provided by Total SA R&D (J.N. Ferry). SAB gratefully acknowledges NERC award NE/R002576/1; Measuring Rates of Weathered Petroleum Accumulation, South China Sea.

Author contributions

M.N, G.M. and S.B. sailed on IODP Expedition 367/368 and are responsible for the sampling of the cores. M.N. and G.M. had the idea to test the thermal imprint of breakup on the SE China COT. A.S. S.C and L.G.G perform the vitrinite measurement and the Raman spectroscopy at Roma Tree University. S.B analysed and modelled biomarkers. A.S and M.N adjusted the 1D thermal models. M.N., G.M., A.S., S.C., L.G.G., S.B. and F.D. have analysed the data and modelling results and all contributed to the redaction of this manuscript.

Supplementary information

Name	Offset (cm)	Depth (m)	**TOC (%wt)**
U1499			
U1499A-8H-4W	130-134	70.054	1.36
U1499A-19X-4W	22-24	167.14	0.5
U1499A-48X-5W	18-22	449.757	0.49
U1499B-2R-2W	120-123	657.71	0.25
U1499B-9R-1W	120-124	724.14	0.18
U1499B-12R-1W	30-34	752.36	0.44
U1499B-27R-4W	30-38	900.86	0.33
U1499B-30R-5W	52-55	932.25	0.32
U1499B-34R-1W	91-96	966.36	0.23
U1499B-37R-1W	115-120	995.66	3.15
U1499B-38R-1W	76-84	1005.04	1.01
U1499B-40R-1W	78-81	1024.41	2.19
U1499B-41R-1W	39-46	1033.76	0.61
U1502			
U1502A-10R-5W	56-60	458.02	0.3
U1502A-14R-3W	12-16	493.36	0.4
U1502A-28R-2W	46-50	626.19	0.53
U1502A-38R-5W	116-118	726.78	0.12
U1502B-4R-1W	47-49	739.15	0.27

SI 1: Determination of TOC (%wt) using the Rock-Eval methodology (Espitallié et al., 1985)

SI 2: Histogram of the vitrinite reflectance data at Site U1499

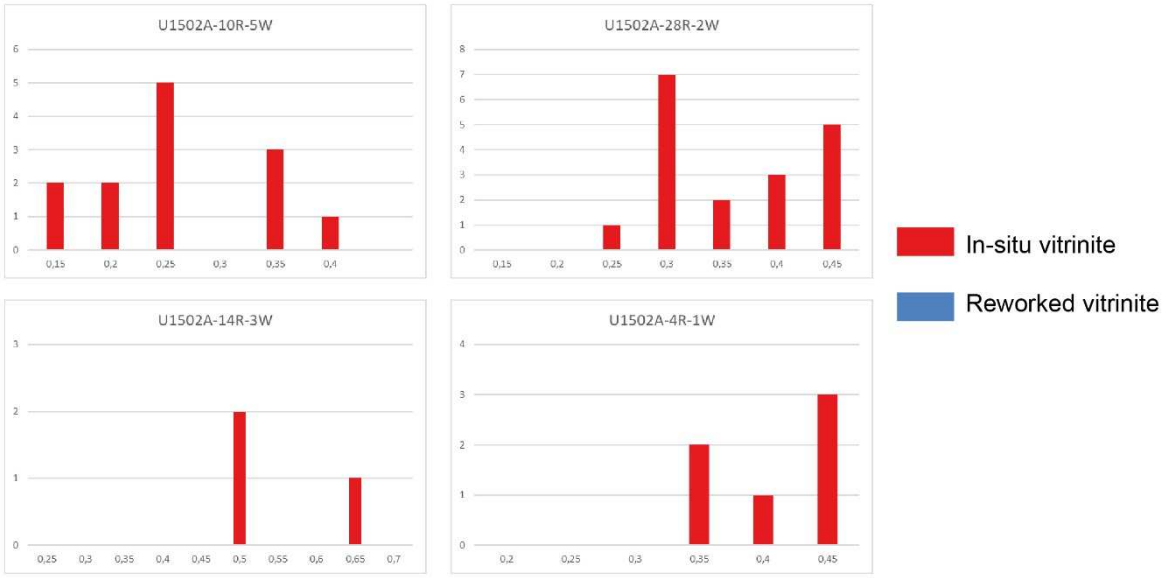

SI 3: Histogram of the vitrinite reflectance data at Site U1502

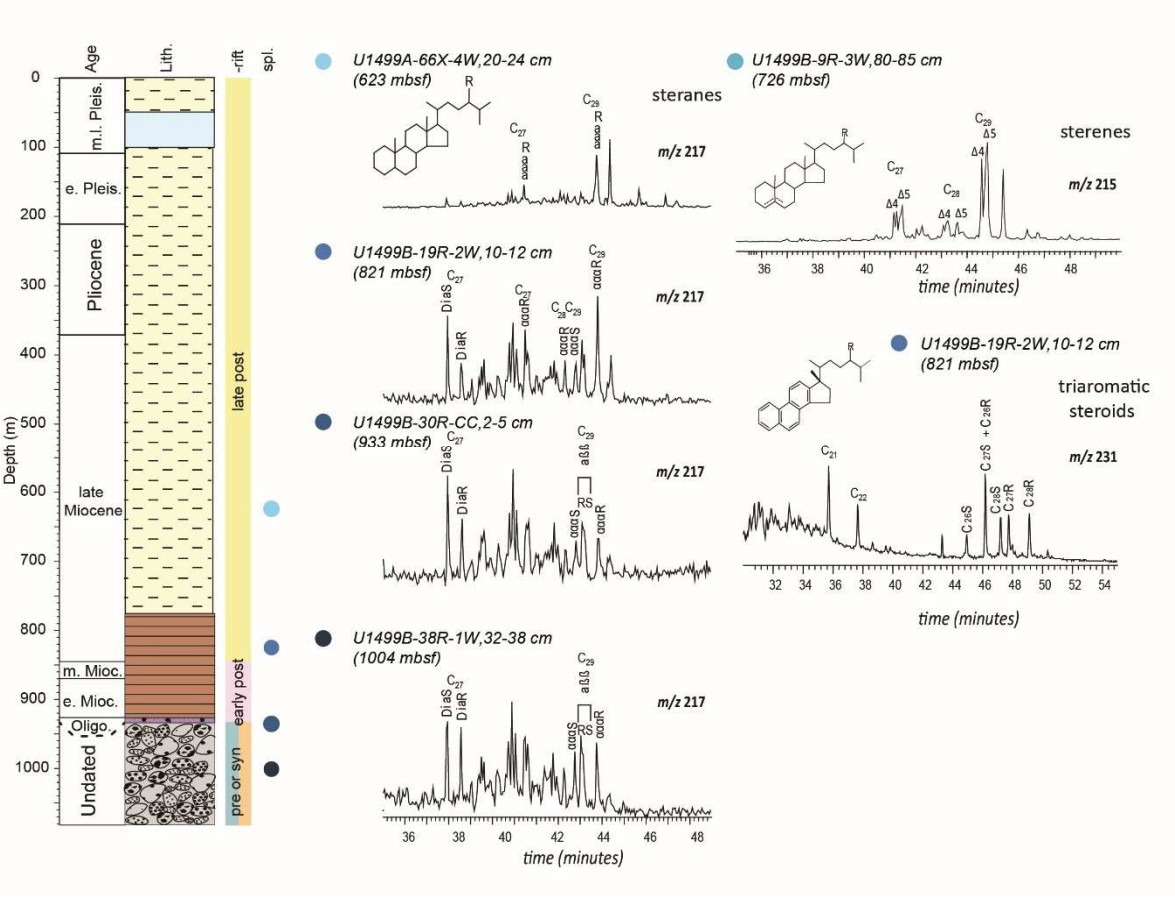

SI 4: Selected ion chromatograms for *m/z 217*, m/z 215 and m/z 231 for samples of Site U1499, showing transition from very early stages of diagenesis (pre-thermal alteration) through to pre-oil window, early oil window and late oil window levels of thermal maturity.

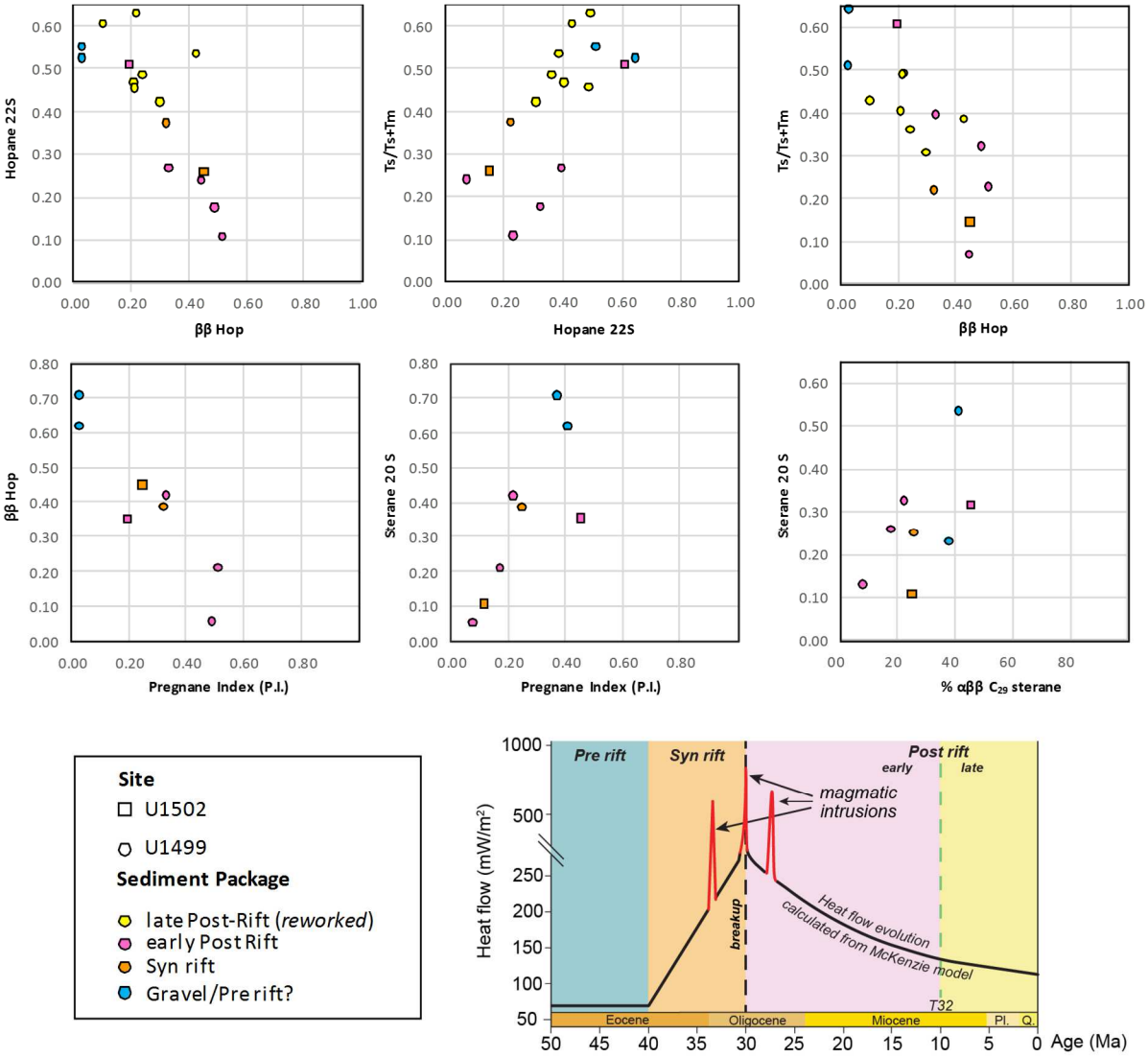

SI 5: Cross plots of thermal maturity parameters listed in Table 3. Colour coding represents sediment packages related to different stages of rifting . Note that the high level of thermal maturity measured for the late post-rift sediment is due to the presence of reworked sedimentary organic matter and that the thermal maturity of these youngest sediments is best gauged by the presence of thermally immature and unstable compounds such as the sterenes, shown in SI 4. The presence of thermally immature and unstable compounds such as sterenes can only be explained by these sediments having not been exposed to high temperatures since their deposition.

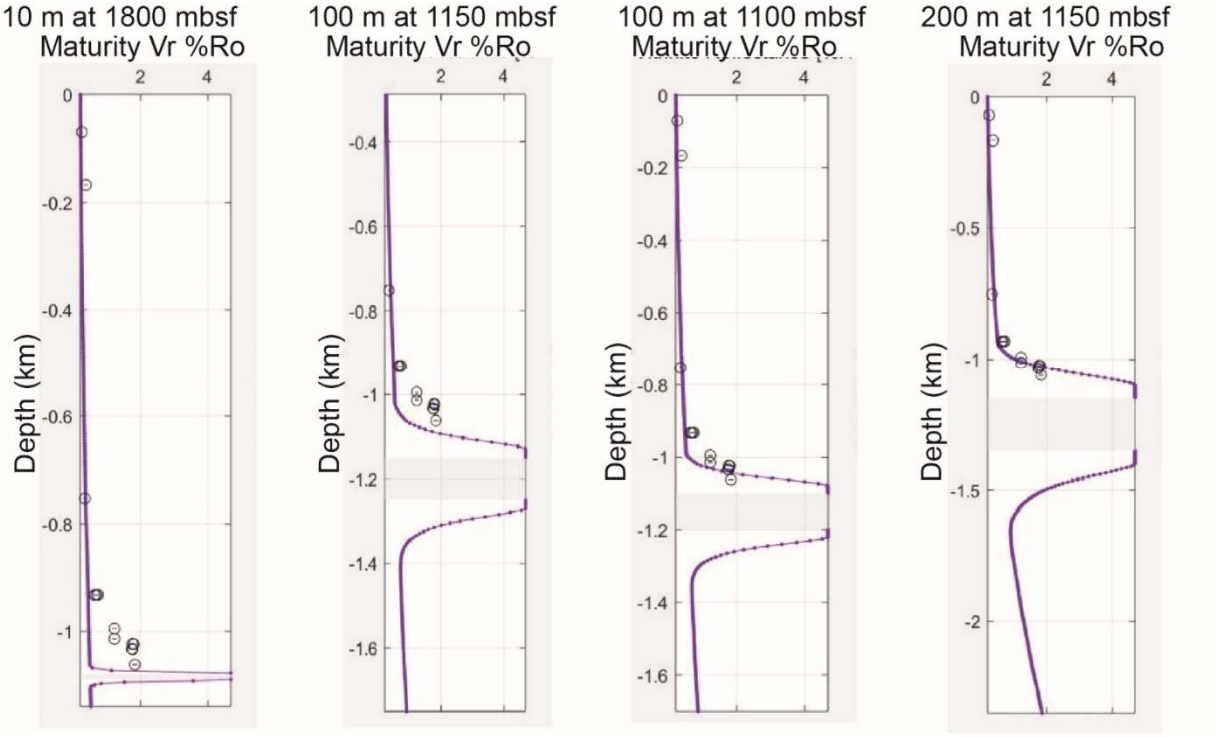

870

871 **SI 6** Selected examples of thermal maturity models perform with the SILLi 1.0 software (Iyer et al.,
872 2018) for different sill intrusion thickness and depth.

873

874

875 **SI References**

876 ASTM D7708-14, Standard Test Method for Microscopical Determination of the Reflectance of
877 Vitrinite Dispersed in Sedimentary Rocks, ASTM International, West Conshohocken, PA, 2014,
878 www.astm.org

879 Espitalié, J., Deroo, G., Marquis, F., 1985. La pyrolyse Rock-Eval et ses applications. Première
880 partie. Revue de l'Institut français du Pétrole 40, 73–89

881 Iyer, K., Svensen, H., Schmid, D.W., 2018. SILLi 1.0: A 1-D numerical tool quantifying the
882 thermal effects of sill intrusions. Geosci. Model Dev. 11, 43–60.
883 https://doi.org/10.5194/gmd-11-43-2018

884